DYNAMICS OF EARTH'S MAGNETOPAUSE DURING SOLAR STORMS: INSIGHTS FROM IN-SITU MEASUREMENTS OF NASA'S MMS MISSION

MSc Astronomy Thesis

By:
Amar Deep



DEPARTMENT OF ASTRONOMY , ASTROPHYSICS AND SPACE ENGINEERING

INDIAN INSTITUTE OF TECHNOLOGY INDORE

May, 2025

DYNAMICS OF EARTH'S MAGNETOPAUSE DURING SOLAR STORMS: INSIGHTS FROM IN-SITU MEASUREMENTS OF NASA'S MMS MISSION

A THESIS

Submitted in partial fulfilment of the requirements for the award of the degree

of

Master of Science in Astronomy

by

Amar Deep



DEPARTMENT OF ASTRONOMY, ASTROPHYSICS AND SPACE ENGINEERING

INDIAN INSTITUTE OF TECHNOLOGY INDORE

May, 2025



INDIAN INSTITUTE OF TECHNOLOGY INDORE

CANDIDATE'S DECLARATION

I hereby certify that the work which is being presented in the thesis entitled **DYNAMICS OF EARTH'S MAGNETOPAUSE DURING SOLAR STORMS: INSIGHTS FROM IN-SITU MEASUREMENTS OF NASA'S MMS MISSION** in the partial fulfillment of the requirements for the award of the degree of **MASTER OF SCIENCE** and submitted in the **Astronomy, Astrophysics and Space Engineering , Indian Institute of Technology Indore,** is an authentic record of my own work carried out during the time period from July-2023 to June-2025 under the supervision of Prof.Abhirup Datta.

The matter presented in this thesis has not been submitted by me for the award of any other degree of this or any other institute.

Adeep 12/05/25

Signature of the student with date (NAME OF THE M.Sc. STUDENT)

This is to certify that the above statement made by the candidate is correct to the best of my/our knowledge.

Signature of the Supervisor of M.Sc. thesis (with date)

(NAME OF SUPERVISOR)

Shwante

Amar Deep has successfully given his/her M.Sc. Oral Examination held on 06/05/2025.

Signature(s) of Supervisor(s) of MSc thesis

Date:

Convenor, DPGC Date: 19/05/2025

Mansueta Chakrakorty

Manuela Chakrakoty Programme Coordinator, M.Sc.

Date: 19/05/2025

HoD, DAASE

Date:

ACKNOWLEDGEMENT

I would like to express my heartfelt gratitude to my supervisor, Prof. Abhirup Datta, for his invaluable guidance and for providing me with the opportunity to contribute to this project. His unwavering support, encouragement, and belief in my abilities, especially during challenging times, have been instrumental in my journey.

I am thankful to Mr. Keshav Aggarwal and Mr. Bhuvnesh Brawar for their mentorship and guidance throughout the course of my work. Their insights greatly helped me strengthen my understanding of the project and improve my contributions. I would also like to extend my sincere thanks to all my labmates for fostering such a supportive and positive environment. Their patience and understanding, especially toward my reserved nature, are truly appreciated.

This journey would have been far more difficult without the steadfast support of my batchmates Vijay, Prasad, Gitaj, Vishrut, Parth, and many others. I am very much thankful to my dear friends Akash, Vivek, Prashant, and Ashish for their constant encouragement, camaraderie, and friendship. Your presence has made every challenge easier and every success more meaningful. Thank you all for being such an important part of my life and for making this experience unforgettable

I am deeply thankful to my mother and sister for their trust, encouragement, and for giving me the opportunity to leave home, while they managed everything at home on their own without any concerns. A special thanks to my father, who is not with us, but whose way of thinking continues to inspire me with positivity.

Finally, I would like to express my sincere gratitude to the Department of Astronomy, Astrophysics, and Space Engineering for providing me with the opportunity to engage in such a fascinating area of research. I am also thankful to IIT Indore for offering me a strong academic foundation and equipping me with the skills necessary to navigate real-world challenges.

ABSTRACT

The Earth's magnetosphere works as a protective shield against highly magnetized and energetic plasma originating from the Sun. This solar wind energy is transferred into the magnetosphere through various mechanisms, like magnetic diffusion, reconnection, and plasma instabilities. Our study focuses on the response of the magnetopause the outer boundary of the Earth's magnetosphere, to varying solar wind conditions. To investigate this, we employed advanced analytical techniques such as Minimum Variance Analysis to get the magnetopause and to project the magnetic field components during boundary crossings. A semi-automated Python-based pipeline was developed to identify magnetopause crossings by detecting abrupt changes in magnetic field and energy spectra. Additionally, the empirical Shue98 model was used to estimate the shape of the magnetopause and standoff distance.

Our results indicate significant compression of the magnetopause toward Earth during intense solar storm events, such as "Mother's Day Storm" of May 2024. During this event, the magnetopause was observed as close as 6.48 Earth radii (Re) from Earth's center, compared to 11.08 Re on a typical quiet day, indicating a compression of over 3.5 Re compare to the standoff distance of magnetopause. These displacements were accompanied by notable variations in magnetic field, electron density, temperature, and velocity, as recorded by MMS spacecraft. Over a three-year period, we have identified 297 magnetopause crossings using the developed detection pipeline. For each crossing, we extracted corresponding plasma parameters, providing an opportunity to analyze the physical processes occurring near the magnetopause. The plasma data revealed a redistribution of plasma flux, with lower density and velocity near subsolar region, and higher values toward the dusk and dawn flanks of the magnetopause.

Finally, we validated the detected magnetopause locations by comparing in situ data from the Wind satellite with the predicted positions from the Shue98 model. The observed locations matched well within an error margin of ± 1 Re, demonstrating the accuracy and reliability of our detection method.

Contents

Li	List of Figures			VI
Li	st of T	Tables		X
1	Introduction			1
	1.1	Space	Weather	1
	1.2	Magne	tosphere of Earth	2
		1.2.1	Bow shock	4
		1.2.2	Magnetosheath	7
		1.2.3	Magnetopause	9
		1.2.4	Magnetopause Current	11
		1.2.5	Magnetopause Location	11
		1.2.6	Solar wind Interaction with the Earth Magnetopause	13
	1.3	Energy	transportation In the Earth Magnetosphere	15
		1.3.1	Magnetic Reconnection	15
		1.3.2	Kelvin Helmholz Instability(KHI)	17
		1.3.3	Diffusion	17
	1.4 Impacts of space weather on Space Operations and Tech-			
		nology	·	19
2	Ove	rview O	of MMS Satellites	21
	2.1	Spaced	eraft and Instruments	21
		2.1.1	Fluxgate Magnetometer	22
		2.1.2	Fast Plasma Investigation	24
		2.1.3	Hot Plasma Composition Analyzer	26
	2.2 Spacecraft Orbit and Data Collection			27
		2 2 1	MMS Data Levels	28

	2.3	Wind Satellite	29
		2.3.1 Wind Magnetic Fields Investigation (MFI)	30
		2.3.2 Solar Wind Experiment (SWE) on Wind Spacecraft .	31
3	Observation and Data Analysis		
	3.1	Minimum Variance Analysis	34
	3.2	Detection of the Magnetopause	35
	3.3	Magnetopause Model	37
4	Results and Discussion		
	4.1	Magnetopause Identification	39
		4.1.1 Non Storm Day Magnetopause	40
		4.1.2 Storm Day Magnetopause	43
	4.2	Structure of the Earth Magnetopause	49
	4.3	Plasma Parameters Values	51
	4.4	Magnetopause Crossing Validation	55
5	Summary		
	5.1	Future Aspects	59
Bi	bliog	raphy	60

List of Figures

1.1	Earth Magnetosphere and Its parts are shown (Image credit	
	: Wikimedia Commons)	3
1.2	Figure shows Quasi Parallel and Perpendicular Bow shock .	5
1.3	Planetary Bow Shocks of our planet's Solar system [Spreiter and Stahara, 1995]	6
1.4	Plasma tube and plasma depletion model which calculates the number density as the tube approaches the Magnetopause ([Zwan and Wolf, 1976])	8
1.5	First Observation made by Explorer-XII, A change in the Magnetic field occurs at $8.2R_e$. (credit:([Cahill and Amazeen, 1963])	10
1.6	schematic illustration of charge particles trajectory in the Magnetosheath. In the upper one, a polarization field is present below which is neutralized(credit: [Willis, 1975]).	12
1.7	First Magnetic field graphs are the magnetic field component in the minimum and Maximum Variance direction, the magnetic field Bz component, and all Magnetic field com-	
1.8	ponents respectively	12
1.9	credit of J. Jokipii, University of Arizona)	14 16
1.10	Kevin Helmholtz Instability around Earth Magnetosphere [Sorathia et al., 2020]	17
2.1	Fluxgate Magnetometer(credit: Supratik Banerjee)	23

2.2	Top hat Analyzer Systematic diagram [Hirahara et al., 2023] 25
2.3	Hot Plasma Composition Analyzer schematic diagram with the trajectory of Ions(credit to D.T. Young et al
2.4	MMS Satellite Orbits During Different Phases. The orbits are in GSE coordinates in the x-y plane. (Credits: NASA/SwRI) 27
2.5	MMS satellite orbit and Region of Interest(ROI) where satellite instruments work and collect the data
3.1	Magnetic Field Components are shown, the vertical line that detects the fluctuation in the data
3.2	Data of the FPI Instrument are shown, plasma parameters and vertical lines with the fluctuation detected by the algorithm
4.1	The Figure shows Dst, Kp, and AE Index Variation of four Days. Starting from 2 May to 5 May 2024 40
4.2	MMS1 Fluxgate magnetometer data of Magnetic field First two figures are the magnetic field component in the direction of minimum and maximum variance direction, and the last plot includes the magnetic field X, Y, Z components in GSE coordinate and time in UTC format
4.3	Spacecraft orbit in X-Y plane In GSE, the calculated Magnetopause and spacecraft location at different times are shown. The red star in orbit is the SC location at the time of crossing
4.4	MMS1 FPI Instrument Measurement number density of Ions Temperature Velocity Vectors and Energy spectrum. The vertical dashed line indicates the starting of the Magnetosheath, current sheet, and Magnetopause crossing(left-to-right lines) and the time shown in UTC formate
4.5	Coronal Mass Ejection occurred on May 7-8 are shown, Images from LASCO C2 and C3 Filters
4.6	The variation of DST, Kp, and AE Index is shown on 11-May, starting from 9-15 May 2024

4.7	MMS1 Fluxgate magnetometer data of Magnetic field First two figures are the magnetic field component in the direction of minimum and maximum variance direction and the last plot includes the magnetic field X, Y, Z components in GSE coordinate and time in UTC format.	47
4.8	MMS fpi measurements of number density of electron, temperature of electron parallel and perpendicular to magnetic field, velocity X component and velocity X, Y, Z components(all quantities are in GSE) and energy spectrum	48
4.9	The Magnetopause compression shown during the storm comparison to the standoff distance (10Re), the compression is 3.51 Re. The light blue is the orbit of the satellite, and stars show the satellite's position at different timestamps and time in UTC format.	48
4.10	Plot of MMS1 Satellite orbit data of 10 months shows that the satellite covers the X-Y plane	49
4.11	Each Point shows a Magnetopause crossing, and the corresponding color shows the time of that crossing, which is shown on the colorbar.	50
4.12	Scattered points are in the location of Magnetopause crossings and color represents the intensity of the Magnetic field. The left plot is for the magnetic field x component, and the right one is for the y component of the magnetic field	51
4.13	Scatter point locations are in the crossing coordinates location, and color represents the magnitude of the velocity $x(left)$ and $y(right)$ component	52
4.14	Temperature of the Ions perpendicular and parallel to the magnetic field is shown at the time and location of the Magnetopause crossing	53
4.15	The number Density of the Ions shown at the time and location of crossing	53
4.16	Values of the Plasma Parameters at the time of crossings	

4.17	The x-axis represents "Difference in R0 (Re)" which mea-	
	sures the discrepancy between observed Magnetopause cross-	
	ings and those predicted by the Shue model	56

List of Tables

4.1	Daily sunspot numbers and their corresponding sizes (in	
	MH) for May 2024 Storm(credit to NOAA SWPC	44
4.2	Halo CMEs: Date, Time, Angular Width, and Speed Be-	
	tween 5-15 May 2024. These CMEs' Information is taken	
	by LASCO	44
4.3	MP location, MP Difference, which is calculated based on	
	the standoff distance of the Magnetopause and spacecraft	
	location during MP crossing location	49

Chapter 1

Introduction

1.1 Space Weather

Space weather is the dynamic state of the interconnected space environment, influenced by variable conditions on the Sun and in the outer atmosphere. It encompasses phenomena that can directly or indirectly impact human activities and affect the operation of satellites and ground-based technological systems [Baker, 1998].

From the Carrington Event on September 1, 1859, to the loss of Starlink satellites on February 4, 2022 [Dang et al., 2022], space weather has remained a critical and evolving field of study. Numerous significant incidents have occurred, including two severe to extreme solar storms in 1972 and 1989, which caused widespread disruptions to electrical and communication grids across North America and Quebec. In another instance, a strong geomagnetic storm in November 2015 led to the temporary disappearance of flights from Sweden's air traffic control radar for over an hour. These events highlight the vulnerability of our technology-dependent society to the effects of space weather.

The Sun is the main source of space weather. It continuously emits radiation and streams of charged particles, primarily protons and electrons, collectively known as the solar wind. The movement of this outflow is caused by the contrast in temperature between the Sun's surface and the surrounding interplanetary space. However, the solar wind is neither steady nor uniform—it undergoes constant fluctuations. These variations affect Earth's

space environment in various ways, such as generating high-energy radiation that interacts with the upper atmosphere to produce auroras, and inducing electrical currents that can interfere with satellite navigation, power grids, and communication systems.

Approximately every 11 years, the Sun reaches a phase of maximum activity in its solar cycle. During this period, it frequently erupts, releasing vast quantities of plasma into the solar atmosphere in events known as coronal mass ejections (CMEs). A single CME can carry up to 10^{12} kg of material—equivalent to the mass of around a quarter of a million aircraft carriers—and can travel at speeds exceeding 1000 km/s. When these CMEs are directed toward Earth, they can trigger powerful solar storms that significantly impact the planet's space and ground-based systems.

1.2 Magnetosphere of Earth

The Earth's magnetosphere is an area surrounding the planet where magnetic field of the Earth is stronger than the magnetic influences from outer space. This zone encompasses several important regions, such as the magnetosheath, the bow shock and the magnetopause. [Heikkila, 2011].

In the early 1970s, scientific investigations into Earth's space environment revealed that processes such as magnetic reconnection play a key role in the interaction between the solar wind and Earth's magnetosphere. Magnetic reconnection occurs when the magnetic field carried by the solar wind connects with Earth's magnetic field, particularly when their directions are nearly opposite. This process enables energy, mass, and momentum from the solar wind to be transferred into the magnetosphere, significantly influencing its dynamics. As a result of this interaction, the outer regions of the magnetosphere are stretched and forced to flow away from the Sun, forming a long magnetotail that extends in the anti-Sunward direction[Dungey, 1961].

Magnetospheric Convection

Magnetospheric convection describes the large-scale movement of plasma within the Earth's magnetosphere. This circulation includes a return flow

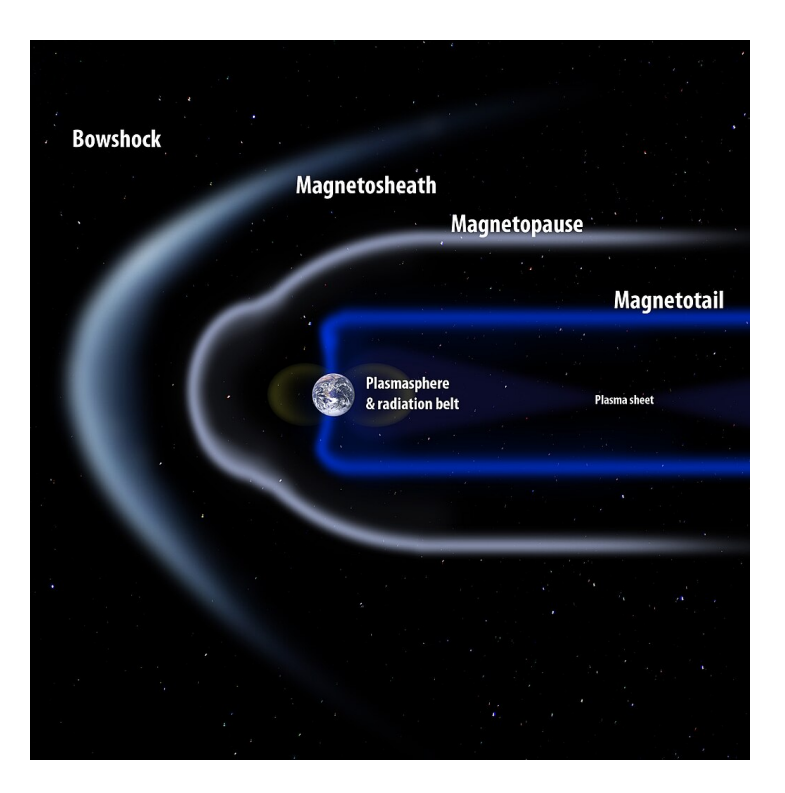


Figure 1.1: Earth Magnetosphere and Its parts are shown (Image credit: Wikimedia Commons)

directed toward the Sun along closed magnetic field lines in the inner magnetosphere, which establishes a dawn-to-dusk electric field across the entire magnetotail. Initially, the concept of magnetospheric convection was met with skepticism due to the scarcity of direct observational data. Over time, however, it gained acceptance thanks to evidence from ionospheric convection patterns and spacecraft detections of the dawn-to-dusk electric field in regions such as the polar caps and auroral zones.

Early theoretical models proposed that this electric field resulted from a combination of two components: a uniform dawn-to-dusk field in the equatorial plane of the magnetosphere and an inward-pointing radial electric field produced by Earth's rotation. In such an electromagnetic configuration, low-energy charged particles experience $E \times B$ drift, moving along paths that align with the electric potential contours.

The Alfvén layer marks the boundary between two different types of particle drift paths: open trajectories that stretch from the magnetotail to the dayside magnetopause, and closed paths that loop around the Earth. On the dusk side of the magnetosphere, the Sunward plasma convection counters

the eastward co-rotation, forming a stagnation point. On the dawn side, these motions are additive. This results in slower flow speeds on the dusk side within the Alfvén layer, causing a wider spacing of equipotential lines. Therefore, for low-energy particles, the Alfvén layer lies farthest from Earth near the dawn region.

1.2.1 Bow shock

When the supersonic solar wind collides with Earth's magnetosphere, it generates a shock wave. This interaction compresses the magnetosphere on the dayside while stretching it into an elongated teardrop shape on the nightside. The resulting shock wave, known as the bow shock, leads to notable changes, including increased plasma density and temperature, enhanced magnetic field, and a transition from supersonic to subsonic flow. The local structure of the bow shock depends on the angle between the shock normal and the direction of the interplanetary magnetic field carried by the solar wind. A perpendicular bow shock ($\theta = 90$) is a sudden change in plasma properties in a small area. A parallel shock is not a shock in the classical sense, but rather a broad transition embedded in high-amplitude turbulence. There are two types of shocks: quasi perpendicular and quasiparallel shock(figure(1.2). The bow shock can accelerate charged particles in the Sunward direction along with Magnetic field lines, then the Solar wind sweeps them back, forming a foreshock boundary in which protons with a given velocity parallel to the Magnetic field are found.

The bow shock is observed in the high-speed Solar wind of every planet other than Pluto. Planets' BS nose varies from the $1.4R_{\nu}$ (Rv is the radius of Venus) to 88Rj (Rj is the Radius of Jupiter). The Bow shock of the Earth and Venus is observed most extensively. BS is the region where the plasma properties change abruptly, and the flow of Solar wind changes the supersonic. Venus not have a Magnetosphere, but it has a sufficiently thick Ionosphere, which creates the Ionopause. A few conditions are required to generate a bow shock. First, Solar wind coming from the Sun has highly conducting properties, allowing for the interactions of the particles in the absence of direct collisions, as occurs in a Non-Ionized gas. Second, the speed of the Solar wind should be supersonic. The third one is Solar wind should be de-

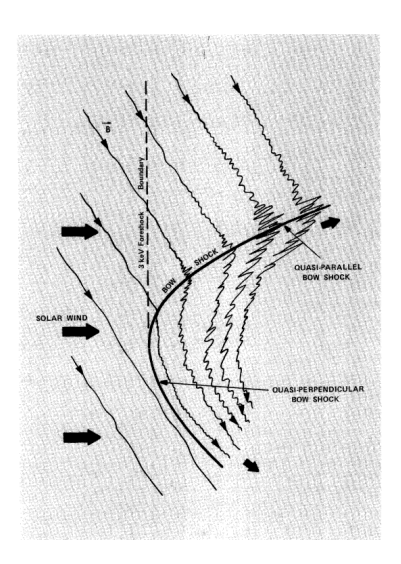


Figure 1.2: Figure shows Quasi Parallel and Perpendicular Bow shock

flected around the planet, either by the Magnetopause or by the Ionopause; this will create an obstacle for the Solar wind other than the planet. If this obstacle is not created, then Solar wind directly interacts with the planet and is absorbed by it. The planets Earth, Mercury, Jupiter, Saturn, Uranus, and Neptune have obstacles because of their magnetic field, and Mars and Venus have the Ionospheric Obstacle. The function of bow shock is to deflect the plasma upward and downward to the planet.

Earth's bow shock is a boundary formed where supersonic Solar wind collides with Earth's magnetic field. Because of this interaction collision-less shock wave serves as a critical protective mechanism, slowing and deflecting the Solar wind around the Magnetosphere. Unlike subsonic flows, where gradual pressure gradients can adjust the plasma's trajectory, the Solar wind's high speed (Mach number 8) exceeds the propagation speed of pressure waves, necessitating a sudden transition. The shock converts the Solar wind's kinetic energy, represented by its dynamic pressure (proportional to density times velocity squared), into thermal and magnetic pressure through compression and heating. This process creates a subsonic flow downstream, allowing static pressure gradients to further deflect the plasma around Earth's magnetic shield. The shock's structure and position depend on the balance between the Solar wind's ram pressure and the Magnetosphere's resistance. Compression ratios vary based on the plasma's thermodynamic properties: a polytropic index of 5/3 (typical for adiabatic

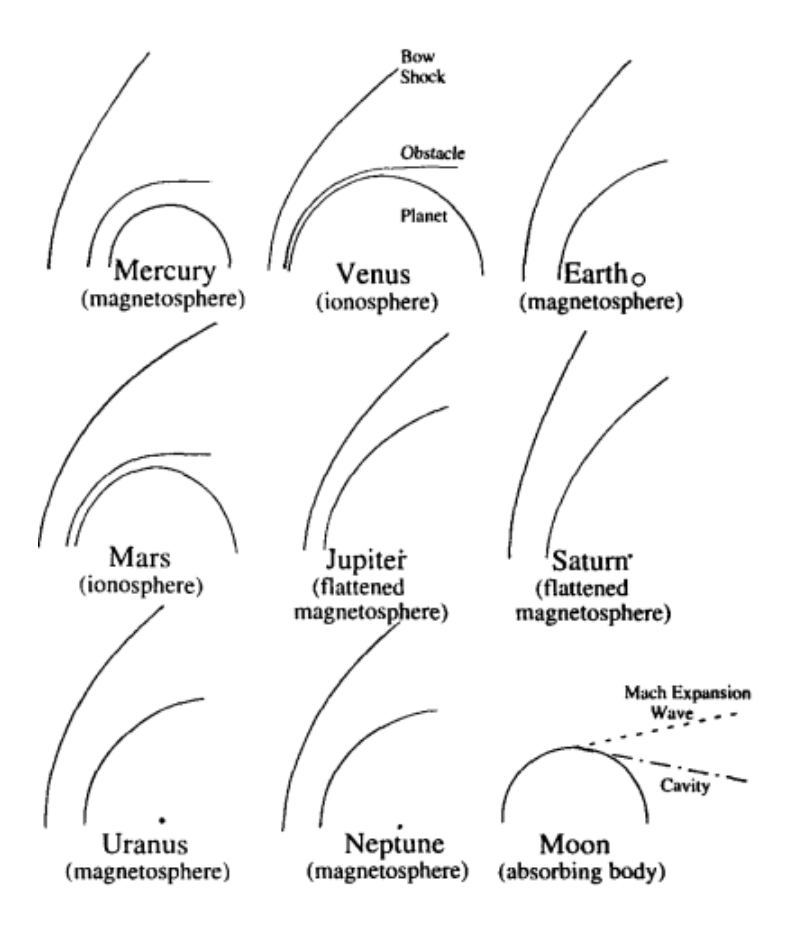


Figure 1.3: Planetary Bow Shocks of our planet's Solar system [Spreiter and Stahara, 1995]

monatomic gases) allows compression by a factor of \approx 4 [Petrinec, 2002],[Behar et al., 2024] while magnetized plasmas with two-dimensional heating (index 2) compress by 3. The shock's standoff distance from Earth adjusts dynamically, influenced by Solar wind velocity, density, and interplanetary magnetic field strength. For instance, if Solar wind density drops below 0.1 cm³ or the magnetic field exceeds 40 nT, the shock weakens and retreats, potentially dissolving entirely.

The bow shock is not static. It exhibits transient behavior, such as fore-shock regions where reflected particles generate ultra-low frequency (ULF) waves. These waves interact with the shock, periodically reshaping its front and modulating energy transfer [Turc et al., 2023]. Recent studies highlight its role in transmitting wave energy into the Magnetosphere, influencing space weather. High-resolution observations also reveal shock "reforma-

tion," where cyclic interactions with upstream waves create periodic density and magnetic field fluctuations. This dynamic interplay underscores the bow shock's complexity as both a thermalizing boundary and a mediator of coupling between solar wind and magnetosphere.

1.2.2 Magnetosheath

The region situated between the bow shock and the magnetopause is referred to as the magnetosheath (Fig: 1.1). Due to the curved structure of the magnetopause, this zone exhibits considerable large-scale spatial variation in plasma characteristics. Changes in solar wind conditions further contribute to this variability, influencing plasma density, speed, magnetic field and temperature. The orientation of the bow shock—whether it is quasiparallel or quasiperpendicular—also affects these plasma properties [Lucek et al., 2005]. Typically, a quasi-perpendicular shock results in more turbulent behavior within the magnetosheath.

The term "magnetosheath" was first introduced in 1963 [Dessler and Fejer, 1963]. Descriptions from that time regarding the bow shock and magnetopause locations are remarkably consistent with modern interpretations. The initial observations of this region were first observed by the Pioneer-1 mission [Sonett and Abrams, 1963], which reported it as a "shocklike disturbance" characterized by abrupt and significant shifts in the magnetic field direction. This study also marked the first use of the term "magnetopause." Shortly afterward, it became evident that the magnetic field performs a crucial role in plasma behavior within the magnetosheath [Midgley and Davis Jr, 1963].

The magnetosheath was first analytically modeled and numerically examined by [Zwan and Wolf, 1976], whose framework, though primarily one-dimensional, incorporated essential three-dimensional dynamics. Their approach utilizes conservation laws within a magnetic flux tube extending between the bow shock and magnetopause. In this system, the second dimension captures the flux tube's temporal evolution. The third dimension operates in the plane defined by the magnetic field and electric potential gradient, adhering to the magnetized plasma's frozen-in condition. This structure maintains the core scientific concepts while enhancing clarity through

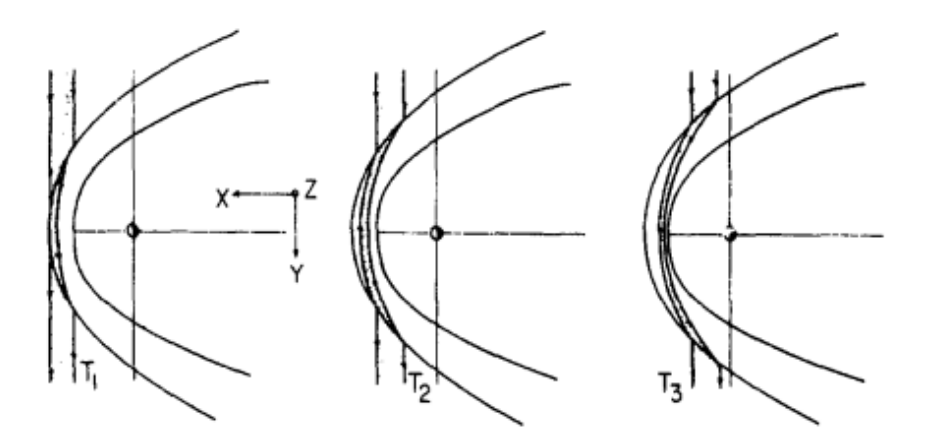


Figure 1.4: Plasma tube and plasma depletion model which calculates the number density as the tube approaches the Magnetopause ([Zwan and Wolf, 1976])

concise phrasing and logical formatting.

There are two main ways plasma is lost or moved around inside the flux tube. First, when plasma hits the bow shock, its flow is redirected, causing it to travel along the magnetic field lines and move away from the main flow path. However, this process by itself doesn't fully explain why plasma is depleted. The second factor comes into play as the flux tube gets closer to the magnetopause: it gets squeezed, which increases the plasma density and slows down the flow. This deceleration is directly tied to the degree of compression. In areas where redirection dominates over deceleration, plasma density tends to drop.

The second key mechanism is familiar "squeezing" effect occurring close to the magnetopause, where elevated pressure levels demand a reduction in plasma pressure to maintain equilibrium. This pressure adjustment expels plasma from the area, analogous to squeezing toothpaste from a tube although this metaphor doesn't specify the physical source of the squeezing force. Each flux tube is naturally embedded within a bundle of neighboring tubes, influencing its dynamics.

In their analysis, [Zwan and Wolf, 1976] present a mathematical solution that allows for a seamless transition between these two depletion processes, made possible by applying an appropriate jump condition. Their model predicts a continuous decline in plasma density from the bow shock to the magnetopause, with the sharpest drop—and a simultaneous increase

in magnetic field strength—occurring just before the magnetopause. This boundary region is identified as the Plasma Depletion Layer (PDL), which they interpret as a manifestation of a slow-mode rarefaction wave.

First Observation of Magnetosheath

The density profile of the Magnetosheath remained poorly understood until the study by [Song et al., 1990]. By analyzing satellite crossings near the Sun-Earth line, they discovered that the plasma density within the Magnetosheath remains relatively constant, with abrupt changes occurring near its outer boundary close to the Magnetopause.

The Magnetosheath is a dynamic region where a variety of waves are generated, typically with frequencies ranging from 0.01 to 0.1 Hz. There are three primary sources responsible for these wave activities. The first and most significant is the interaction between the solar wind and the Bow Shock. Some solar wind particles are reflected at the Bow Shock and travel upstream, forming a region known as the foreshock. In this region, waves are generated and subsequently convected into the Magnetosheath.

The second source of wave activity originates from plasma instabilities, especially prominent in the outer regions of the magnetosheath, where such instabilities can lead to the amplification of waves. The third source stems from the dynamic interaction between the magnetopause and the magnetosheath. This coupling generates oscillatory waves, as disturbances from the upstream solar winds are partially deflected at the magnetopause, enhancing wave activity within the magnetosheath.

1.2.3 Magnetopause

The magnetopause marks the boundary where Earth's magnetic field is balanced by the interplanetary magnetic field. This boundary is essentially a two-dimensional current sheet formed through the interaction between two different plasma populations—those from Earth's magnetosphere and the solar wind. The concept of the magnetopause as the outer boundary of the magnetosphere was first introduced by Chapman and Ferraro in 1931. Later, in 1963, Cahill and Amazeen provided the first clear observational evidence of the magnetopause using data from the Explorer-XII satellite.

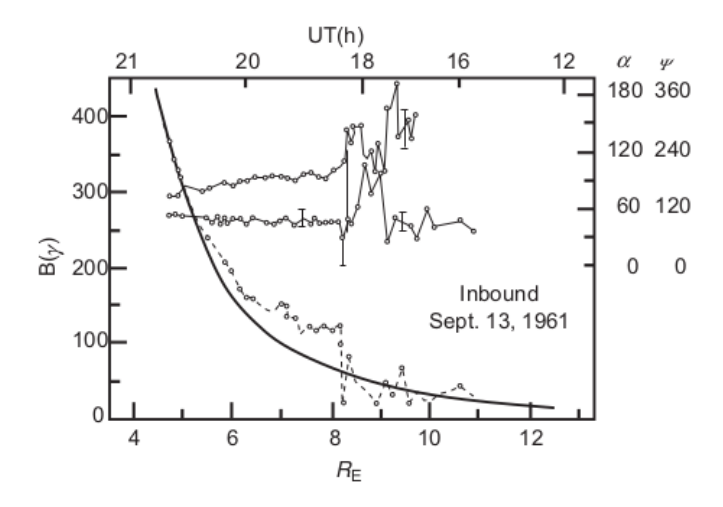


Figure 1.5: First Observation made by Explorer-XII, A change in the Magnetic field occurs at $8.2R_e$. (credit:([Cahill and Amazeen, 1963])

Before reaching $8R_E$, the magnetic field exhibits normal fluctuations, as shown in Figure 1.5. However, at approximately $8.2R_E$, a sudden change in the magnetic field is observed, indicating a crossing of the Magnetopause just inside this boundary. At this point, magnetic field strength nearly doubles, consistent with the presence of a dipolar magnetic field.

As upstream charged particles approach the Magnetopause, they are deflected, generating a surface current near the boundary. This current modifies the magnetic field across the boundary, enhancing it inside and diminishing it outside. If the Magnetopause were an ideal planar surface, this surface current would double the magnetic field on the inside and cancel it completely on the outside.

Chapman and Ferraro analyzed a scenario in which a solar wind stream impinges on the Earth's magnetic field, compressing it into a flat surface. At a distance twice that of this ideal plane, the resulting magnetic field behaves as if produced by an image dipole with the same strength as Earth's dipole field.

Then the Magnetic field is

$$B_{total} = B_{geo} + B_{image}$$

$$B_{total} = \frac{B}{r^3} + \frac{B}{(2R - r)^3}$$

At boundary
$$r = R$$

$$B_{total} = \frac{2B}{R^3}$$

1.2.4 Magnetopause Current

The magnetopause current originates locally from the motion of charged particles—electrons and ions. Because electrons possess a significantly smaller gyro-radius than ions (as shown in Figure 1.6), the overall thickness of the magnetopause is mainly governed by the larger ion gyro-radius. At the boundary layer, the opposing motions of electrons and ions produce a current sheet that forms the dividing line between the magnetosheath and the magnetosphere. This current sheet causes a noticeable change in the magnetic field across the boundary, as illustrated in Figure 1.7.

In Figure 1.7, the blue line marks the onset of the magnetosheath, characterized by fluctuations in the magnetic field. The region between the red and green lines, where the magnetic field reverses, represents the boundary separating the magnetosheath from Earth's magnetopause.

The Magnetopause width is larger than a gyro-radius of the Ions. The reason for this is the effect of plasma, which collects just outside the magnetopause and then redirects upwards and downwards. To better understand the Magnetopause, we should consider these collective effects of the fluid plasma equations.

1.2.5 Magnetopause Location

The Solar wind coming from the Sun has dynamic pressure

$$P_{dynamic} = M_p n_{sw} (V_{sw})^2$$

Where M_p , n_{sw} , V_{sw} are the mass of the proton, the number density of the Solar wind, and Solar wind speed, respectively. The incident Solar wind interacts normally to the Magnetopause surface at the sub-solar point. We have to change this pressure to normal at the magnetopause surface. For this, we have to take the normal direction of the Magnetopause, which can be found using the Minimum variance analysis. Then the dynamic pressure will be

$$P_{dynamic} = \kappa M_p n_{sw} (V_{sw} \cdot n_{mp})^2$$

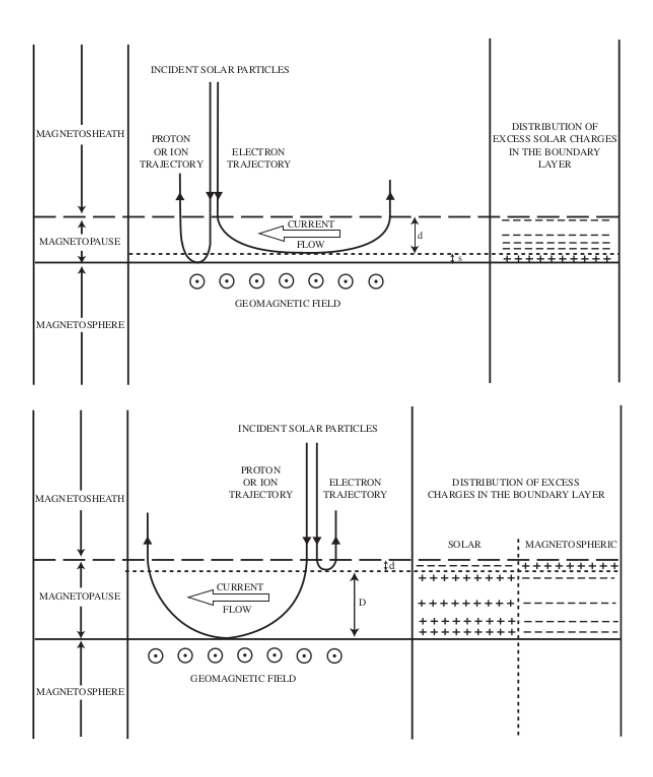


Figure 1.6: schematic illustration of charge particles trajectory in the Magnetosheath. In the upper one, a polarization field is present below which is neutralized(credit: [Willis, 1975]).

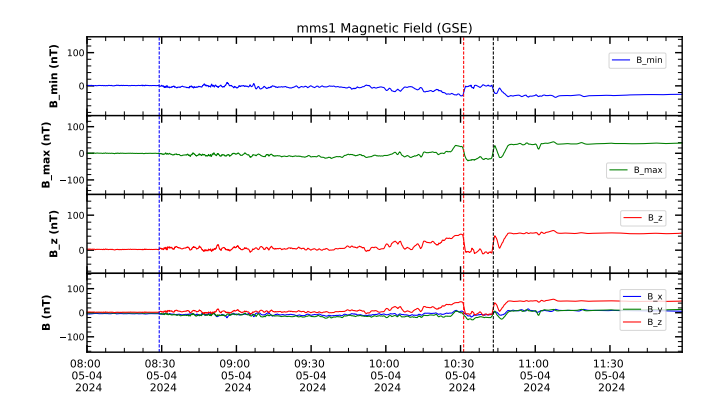


Figure 1.7: First Magnetic field graphs are the magnetic field component in the minimum and Maximum Variance direction, the magnetic field Bz component, and all Magnetic field components respectively.

Where n_{mp} is the normal component of the Magnetopause and takes the account the actual Pressure because the total pressure reduced in the case of three-dimensional upward and downward flow, the Plasma and also the

Solar wind do not reflect ideally.

Inside the Magnetosphere, Magnetic pressure dominates over the thermal pressure and dynamic pressure.

$$P_{msp} = \frac{B_{msp}^2}{2\mu_0}$$

In the case of Pressure Balance

$$\kappa M_p n_{sw} V_{sw}^2 n_{mp} \cos \theta = \frac{B_{msp}^2}{2\mu_0}$$

Here, θ denotes the angle between the Sunward direction and the normal to the magnetopause. In the given equation, the magnetic field is represented as a dipole field, specifically applicable at the subsolar point.

$$M_P n_{sw} V_{sw}^2 = \frac{K B_E^2}{2\mu_0 R_{mp}^6}$$

Where K takes account of deviation from the actual field of the dipole and also takes the κ .then the Magnetopause standoff distance will be

$$R_{mp} = \left[\frac{KB_E^2}{2\mu_0 M_p n_{sw} V_{sw}^2} \right]^{1/6}$$

For Normal Solar wind conditions as $V_{sw} = 400m/s, n = 5cm^{-3}, B_E = 3 \times 10^4 nT, K = 2$, then the calculated Magnetopause distance will be

$$R_{mp} = 9.9 Re$$

1.2.6 Solar wind Interaction with the Earth Magnetopause

As previously noted, the magnetopause is a two-dimensional current sheet maintained by the interaction between two distinct plasma populations: the solar wind and the plasma within Earth's magnetosphere. The solar wind consists of a continuous flow of charged particles—primarily electrons and protons—that are ejected from the Sun with sufficient energy to overcome its gravitational field.

As the solar wind moves outward, it drags the Sun's magnetic field lines along with it. Due to the Sun's rotation, these magnetic field lines form a spiral shape known as Parker's spiral. Since the solar wind is mostly

collisionless, the magnetic field remains "frozen" into the plasma and moves with it, though non-ideal effects may occur.

A comparable scenario occurs near Earth, where its magnetic field acts as a barrier, preventing the solar wind plasma from directly mixing with the magnetospheric plasma. The interface where these two plasma regions meet is known as the magnetopause, which forms a current sheet as a result of the interaction between the Earth's magnetic field and solar wind magnetic field.

The structure and location of the magnetopause are governed by a balance among various pressures: the dynamic pressure from the solar wind's motion, the thermal pressure from particle temperatures, and the magnetic pressure exerted by the fields. This balance shapes the magnetopause into a parabolic form, extending deep into Earth's nightside, reaching distances of up to approximately 200 Earth radii (R_E)

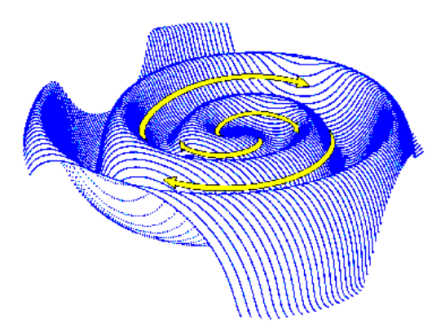


Figure 1.8: Parker's Spiral generated from the Sun is shown.(Image is credit of J. Jokipii, University of Arizona)

A key question in Sun–Earth interactions is how magnetic energy carried by the solar wind is transformed into kinetic energy and transmitted across the magnetopause. The primary process that facilitates this energy transfer is known as magnetic reconnection.

Magnetic reconnection is a fundamental process responsible for releasing stored magnetic energy across various space environments—from the Sun and planets to more distant cosmic systems. At Earth, this phenomenon commonly takes place near the subsolar point of the magnetopause, located in the equatorial plane where the solar wind first encounters Earth's magnetic field.

For reconnection to occur, the interplanetary magnetic field (IMF) attached in the solar wind must oppose Earth's magnetic field direction. When

these opposing fields interact, the frozen-in condition—where magnetic field lines remain bound to the plasma—is disrupted. This disruption allows the field lines from the solar wind and Earth to merge, facilitating the transfer of energy, particles, and momentum across the boundary. This reconnection is enabled by enhanced local plasma resistivity, which permits magnetic energy to be converted into other forms such as particle heating and acceleration.

1.3 Energy transportation In the Earth Magnetosphere

In addition to magnetic reconnection, other mechanisms, like the Kelvin-Helmholtz instability (KHI), can also play a role in transferring energy, mass, and momentum from the solar wind to the Earth's magnetosphere. These processes occur at different locations and under various solar wind conditions.

1.3.1 Magnetic Reconnection

Magnetic reconnection is a highly effective and extensively studied mechanism for transferring energy from the solar wind to the Earth's magnetosphere. When the interplanetary magnetic field (IMF) has a southward component, it can reconnect with the Earth's northward-directed magnetic field near the dayside Magnetopause. This reconnection process forms new magnetic field lines that link the solar wind directly to the Earth's magnetosphere.

Once these field lines are opened, particles can move freely between the magnetosphere and the solar wind along them. The solar wind then drags these open field lines toward the tail, causing magnetic flux to accumulate in the Earth's magnetotail. This accumulation enlarges the magnetotail and stores magnetic energy in the tail lobes.

Therefore, magnetic reconnection on the dayside is a vital process for transferring solar wind energy into the magnetosphere. A similar reconnection process also occurs on the nightside, playing an important role in magnetotail dynamics and substorm activity.

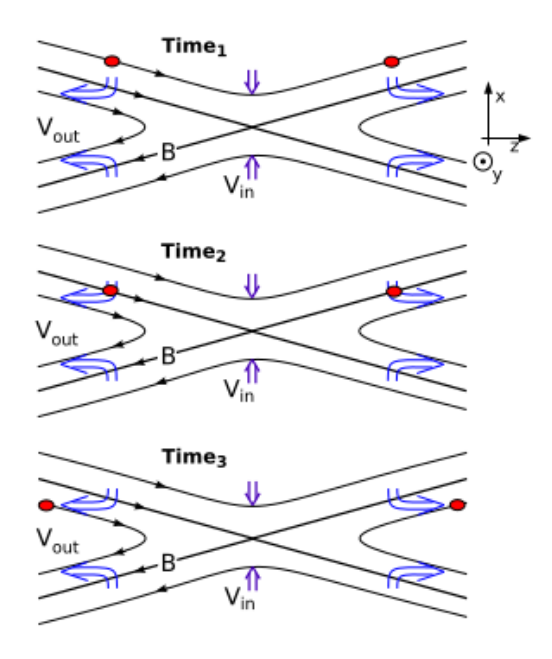


Figure 1.9: Magnetic Reconnection Has been shown in the given plot with the Inward and outward flow of the Plasma

Magnetic reconnection involves the rearrangement of magnetic field lines (or magnetic flux), which necessitates a localized breakdown of Ohm's law, although this occurs in a very small, confined region. Figure 1.9 shows the basic configuration and flow of magnetic flux and plasma during the reconnection process.

The thick magnetic field lines that intersect at the center are called separatrices, and the point where they converge is known as the X-point. In three dimensions, this becomes an X-line. The blue arrows represent the general direction of plasma movement during reconnection.

The regions above and below the separatrices are known as inflow regions, where plasma and magnetic flux move toward the reconnection site. The areas to the left and right are the outflow regions, where reconnected field lines and accelerated plasma are expelled away from the X-point.

Although not strictly required, it is commonly assumed that the plasma far from the reconnection region behaves ideally, that is, the frozen-in condition still applies, and magnetic field lines move with the plasma.

1.3.2 Kelvin Helmholz Instability(KHI)

The interchange motion driven by the Kelvin-Helmholtz instability (KHI) aids in the transfer of momentum through both Maxwell stresses and Reynolds stresses. It also facilitates the exchange of mass and energy by mixing the two distinct plasmas on either side of the Magnetopause.

Kinetic effects, such as finite Larmor radius and ion inertia, allow ions to gyrate across magnetic field lines, enhancing this mixing process. The vortices created by the instability twist the field lines of the Magnetosheath together with those of the Earth's magnetosphere. This interaction leads to the formation of thin current layers and regions with strong velocity shear.

Such transport processes can also lead to the pinching off of magnetic flux "blobs" from the vortex structures. As the instability evolves, the vortices undergo nonlinear growth, where smaller vortices merge into larger ones through a process known as coalescence. This behavior is characteristic of an inverse energy cascade, where energy shifts from smaller to larger spatial scales.

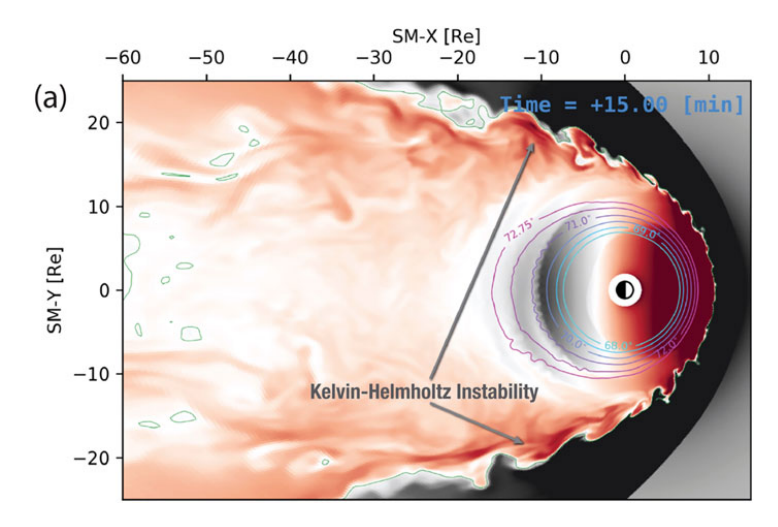


Figure 1.10: Kevin Helmholtz Instability around Earth Magnetosphere [Sorathia et al., 2020]

1.3.3 Diffusion

Plasma can diffuse across magnetic field lines in the direction perpendicular (transverse) to the magnetic field. This behavior is often described by the diffusion equation:

$$\frac{\partial n}{\partial t} = D\nabla^2 n$$

where n is the plasma density and D is the diffusion coefficient. However, this concept remains debated because it depends on localized particle scattering caused by anomalous collisions, which arise from wave–particle interactions.

While theoretical models suggest that diffusion coefficients around $D \approx 10^6 \, \mathrm{m}^2/\mathrm{s}$ are required to explain observed structures like the Low Latitude Boundary Layer (LLBL), exact wave modes responsible for such interactions remain unclear. For instance, simulations of turbulence driven by the Kelvin-Helmholtz instability (KHI) have reported much higher diffusion coefficients, around $D_{\mathrm{diff}} \sim (1-4) \times 10^{11} \, \mathrm{m}^2/\mathrm{s}$ [Nakamura et al., 2022]. These values far exceed earlier estimates, making it difficult to define a clear lower limit for D that is consistent with observations of the Magnetopause's variable thickness (ranging from 100 to 2000 km) [Haaland et al., 2020].

Another challenge is reconciling diffusion with magnetic reconnection processes. Under northward interplanetary magnetic field (IMF) conditions, when reconnection is suppressed, diffusion may become the dominant mechanism for solar wind plasma entry into the magnetosphere. However, observational evidence for classical diffusion remains inconsistent. Magnetopause current sheets often exhibit sharp, well-defined boundaries that contradict expectations from standard diffusion theory [Smets et al., 2007].

This ongoing ambiguity highlights the uncertainty about how plasma transport across the Magnetopause occurs. It remains unclear how much each mechanism whether diffusion, turbulence, or reconnection contributes under varying conditions.

Besides diffusion and reconnection, other proposed energy transfer mechanisms include viscous-like interactions, impulsive penetration, and finite gyro-radius effects. However, magnetic reconnection and turbulence-driven diffusion are considered the two most significant processes.

1.4 Impacts of space weather on Space Operations and Technology

According to the NASA Space Weather Prediction Center, SEPs are one of the primary space hazards. Large SEPs pose a threat to satellite operations and high-frequency radio communication systems. The intensity of these SEP events, which are known as Solar Radiation Storms, is categorized on a scale of 1 to 5, with S1-S5 standing for 10 MeV proton intensity increasing by a factor of 10 from 10pfu to $10^5 pfu$. A total high-frequency radio blackout could occur at $10^5 pfu$.

Numerous examples demonstrate how particle radiation causes significant harm to space missions. Damage to the satellite's Solar panels has also been significant; the primary issue is the decreased efficiency. The anticipated current from the GOES-7 Solar panels decreased by 5–10 percent as a result of the two strong SEP events on September 29, 1989, and October 19, respectively [Gopalswamy, 2024]. Space weather, caused by Solar activity such as Solar flares, coronal mass ejections (CMEs), and bursts of radiation, has significant effects on space operations and technology. These phenomena can disrupt satellites, navigation systems, communication networks, power grids, and aviation, leading to widespread challenges for global infrastructure. Satellites are particularly vulnerable to the effects of space weather. High-energy particles from Solar Storms can damage satellite electronics, causing malfunctions or data errors known as single-event upsets (SEUs). Prolonged radiation exposure also degrades Solar panels and other components, reducing the lifespan of satellites. Geomagnetic Storms can heat the Earth's upper atmosphere, increasing drag on low-Earth orbit (LEO) satellites and accelerating their orbital decay. For instance, during a major Solar Storm in 2024, NASA's ICESat-2 had to enter safe mode to prevent attitude control issues.

Space weather also disrupts navigation and communication systems. Global Navigation Satellite Systems (GNSS), such as GPS, are highly sensitive to ionospheric disturbances caused by Solar activity. These disruptions can delay or scatter radio signals, leading to positioning errors or complete outages lasting up to several days. Such errors affect aviation, maritime

navigation, and critical infrastructure reliant on precise timing. Similarly, high-frequency (HF) radio and satellite communications are often disrupted during Solar Storms due to ionospheric interference, posing challenges for emergency services and military operations.

On Earth, geomagnetic storms can induce strong electrical currents in power lines, known as geomagnetically induced currents (GICs), which can overload transformers and cause widespread power outages. A well-documented example is the 1989 blackout in Quebec caused by a geomagnetic Storm. Aviation is also at risk during intense Solar activity; polar flight routes experience increased radiation exposure for passengers and crew, while aircraft electronics may face disruptions from high-energy particles.

To mitigate these risks, various strategies have been developed. Satellites are being equipped with radiation-resistant components to withstand harsh conditions in space. Power grids are being upgraded with technologies that block harmful currents during geomagnetic Storms. Real-time monitoring systems like NASA's Solar Dynamics Observatory provide early warnings of space weather events. Advances in predictive modelling using artificial intelligence have also improved forecasting accuracy. International cooperation through organizations like the Community Coordinated Modeling Center (CCMC) plays a key role in addressing these challenges.

As the Sun approaches its peak activity during Solar Cycle 25, it is crucial to implement these measures to protect the technologies that are essential for modern life.

Chapter 2

Overview Of MMS Satellites

NASA launched the MMS mission. Its four identical spacecraft are primarily designed to determine reconnection directly in the Magnetosphere and space. Investigate magnetic reconnection in this local natural laboratory to better understand reconnection in other places, such as the sun's atmosphere and neutron stars. To obtain a three-dimensional image of their surroundings, four MMS satellites travel in an adjustable pyramid shape.

2.1 Spacecraft and Instruments

In all four spacecraft, MMS has unique instrument sets. Each of the octagonal-shaped MMS observatories houses eleven scientific experiments composed of twenty-five different sensors. It has an accuracy and time resolution of milliseconds and measures electric fields, magnetic fields, charged velocities, and plasma movement [Baker et al., 2016]. MMS instruments are grouped into three:

- Hot Plasma: To measure the nature of Plasma
- Energetic charged Particles: To measure fast-moving ,energetic particles
- Magnetic Fields and Electric Field: which measures the magnetic fields and electric field.

The Field suite consists of an instrument measuring the electric and magnetic field.

- Search coil Magnetometer (SCM): It takes observation of magnetic field with the frequency of 1Hz-6kHz.
- Flux gate Magnetometer (FGM): It also measures magnetic field with a frequency of 128 sample/s and an accuracy of 0.1nT.
- Electricial double probe: It is a combination of axial double probe, Spin double probe in the frequency range of 100kHz.

The Instrument measuring the particles:

- Fast Plasma Investigation (FPI) It measures the particles' velocity space distribution. It comprises four types of dual Ion Spectrometer (DIS) dual electron spectrometer (DES) on each satellite. FPI adds data of all DES, DIS with time resolution of 30ms and 150ms respectively in the energy range 10eV-30keV.
- Hot Plasma Composition Analyzer (HPCA) provides composition Ions energy distributions of O⁺, H⁺, He⁺⁺, He⁺ in the energy range 1eV - 40keV.
- Energetic Particle Detector (EPD), which consists of the Fly's Eye Energetic Particle Sensor (FEEPS), an all-sky particle sampler, and an Energetic Ion Spectrometer (EIS). They use sampling frequencies of < 10s to measure the angle and energy, composition, and number of ions in the specific energy range 20 keV to 500 keV, and for electrons, 25 keV to 500 keV, and for other ions, it is 45 keV to 500 keV.

2.1.1 Fluxgate Magnetometer

The Magnetospheric Multiscale (MMS) mission relies on high-precision fluxgate magnetometers to study magnetic reconnection in Earth's Magnetosphere. Each MMS spacecraft carries two triaxial fluxgate magnetometers—the Digital Fluxgate (DFG) and Analog Fluxgate (AFG)—to ensure redundancy and avoid single-point failures. These instruments measure magnetic fields with resolutions as low as $8pT/\sqrt{Hz}$ and stability better than 0.1 nT over 100 hours, critical for detecting electron-scale processes

during reconnection events [Russell et al., 2014]. The fluxgate magnetometer operates on the principle of detecting changes in magnetic fields using the nonlinear properties of ferromagnetic materials. At its core, the instrument contains two ring-shaped ferromagnetic cores with high magnetic permeability. These cores are periodically driven into magnetic saturation by an alternating current (AC) excitation signal. In a symmetric magnetic environment, the induced voltage in the sense windings (coils wrapped around the cores) is minimal because the cores saturate evenly.

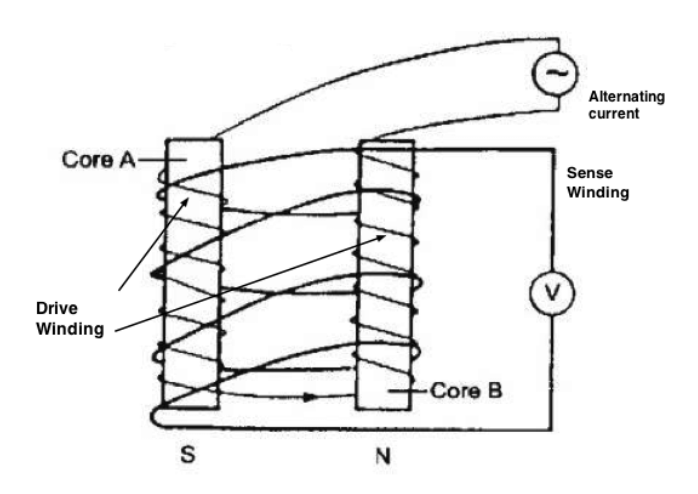


Figure 2.1: Fluxgate Magnetometer(credit: Supratik Banerjee)

When an external magnetic field is present, it biases the cores asymmetrically, causing uneven saturation. This asymmetry generates specific harmonic signals in the sense windings, particularly at twice the excitation frequency (second harmonic). The amplitude of this harmonic signal is directly proportional to the strength of the external magnetic field. The flux-gate magnetometer uses a feedback mechanism to enhance accuracy and dynamic range. The electronics detect the second harmonic signal and generate a counteracting magnetic field through feedback windings. This feedback field cancels out the external field at the sensor location, effectively nullifying it. The amount of current required to produce this feedback field is proportional to the strength of the external magnetic field and serves as the measurement output. Two types of fluxgate magnetometers are commonly used: digital fluxgate (DFG) and analog fluxgate (AFG). Both share similar sensor designs but differ in their electronic processing methods. The DFG

employs advanced digital electronics, including sigma-delta modulators for high-resolution digitization, while the AFG relies on traditional analog circuitry.

The DFG provides superior noise performance and temperature stability, making it ideal for high-precision applications. It uses an application-specific integrated circuit (ASIC) to process signals and achieve low noise levels ($<8pT/\sqrt{Hz}$ at 1 Hz) with dual dynamic ranges ($\pm650nT$ and $\pm10,500nT$). The AFG, on the other hand, offers robust performance with simpler electronics and is often used as a backup system due to its reliability. Calibration is essential for accurate measurements. Ground calibrations determine sensor gains, offsets, and alignment angles under controlled conditions. Inflight calibrations refine these parameters by accounting for environmental factors like temperature fluctuations and spacecraft-generated magnetic fields.

Fluxgate magnetometers are widely used in space missions to study Earth's Magnetosphere and solar wind interactions. Their ability to measure weak magnetic fields with high precision makes them invaluable for understanding phenomena such as magnetic reconnection, which plays a critical role in space weather dynamics.

2.1.2 Fast Plasma Investigation

The Fast Plasma Investigation (FPI) on NASA's MMS mission works by rapidly measuring charged particles (electrons and ions) in space to study how energy is transferred during events like magnetic reconnection. Each spacecraft has sensors (spectrometers) that detect electrons and ions. These particles enter the sensors through small openings. Inside, electric fields (created by charged plates) act like filters. By adjusting the voltage on these plates, only particles with specific energy levels can pass through. For example, a higher voltage lets higher-energy particles through. This process sorts particles into 32 distinct energy levels, like separating marbles by size. The spacecraft spins 3 times per minute.

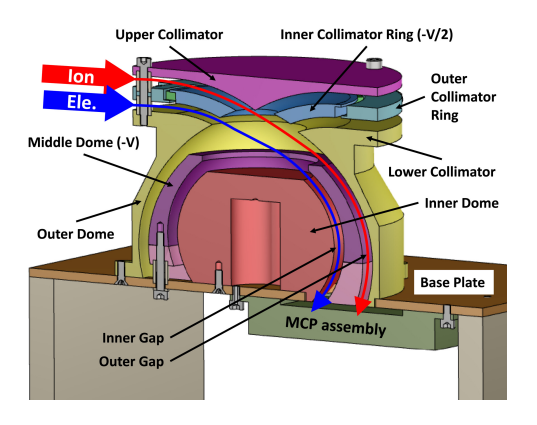


Figure 2.2: Top hat Analyzer Systematic diagram [Hirahara et al., 2023]

As it rotates, the sensors, positioned to face different angles, scan the surrounding space. Each sensor divides the sky into 32 compass-like directions (azimuth) and 16 up-down angles (polar). Over time, this spinning motion lets FPI build a 3D map of where particles are coming from and how they're moving. Electrons are measured every 30 milliseconds (0.03) seconds), while ions are measured every 150 milliseconds (0.15 seconds). This ultra-fast timing is crucial because magnetic reconnection events happen in tiny regions and fractions of a second. FPI's speed ensures no detail is missed. Burst Mode Records data at maximum speed during key events (like reconnection) but stores only short intervals due to limited data storage. Survey Mode continuously records at a slower pace (4.5 seconds per measurement) to provide background context. Building the Full Picture By combining energy, direction, and timing data, FPI calculates how many particles are moving at specific speeds and directions at any moment. These "velocity distributions" show how energy is shuffled between particles and magnetic fields during reconnection. For example, they reveal how electrons get violently accelerated when magnetic field lines snap and reconnect. Redundancy Reliability If one sensor has issues (like on the MMS4 spacecraft), others compensate. The four identical sensors on each spacecraft ensure accurate data even if one partially fails. In short, FPI works like a high-speed camera for space plasma. It sorts particles by energy, tracks their directions as the spacecraft spins, and stitches this data into snapshots of how plasma behaves in real-time. This helps scientists understand how energy explodes in events like magnetic storms, which affect satellites and power grids on Earth.

2.1.3 Hot Plasma Composition Analyzer

It measures the velocity distributions of four key ion species— Hydrogen (H^+) , Helium (He^+) and He^{++} , and oxygen (O^+) —which serve as markers to distinguish between solar wind and terrestrial plasma sources. The HPCA combines electrostatic energy filtering, radiofrequency (RF) dynamic range control, and time-of-flight (TOF) mass spectrometry to achieve high sensitivity and accuracy in extreme plasma environments. The HPCA operates using a two-stage process. First, ions enter through a collimator and pass through an electrostatic analyzer (ESA), which sorts them by energy-tocharge ratio (E/q). The ESA employs a toroidal "tophat" design with concentric shells that apply stepped high voltages (-0.21 V to -7,000 V) to filter ions across a broad energy range (1 eV to 40 keV). To manage the intense proton fluxes encountered in regions like the Magnetopause, the ESA incorporates an RF system that selectively attenuates protons while allowing heavier ions (e.g., O^+) to pass. This RF modulation acts as a low-resolution mass filter, enhancing the instrument's dynamic range and preventing detector saturation. After energy selection, ions are accelerated by a -15 kV po-

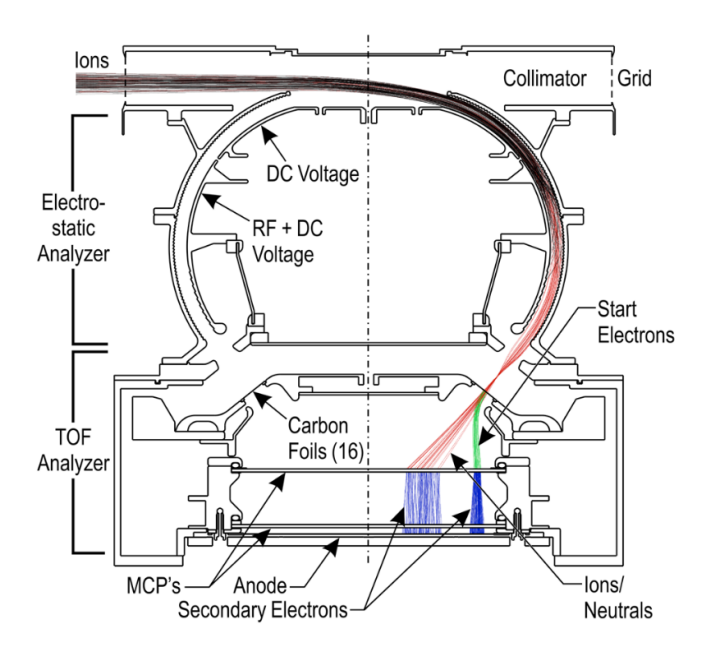


Figure 2.3: Hot Plasma Composition Analyzer schematic diagram with the trajectory of Ions(credit to D.T. Young et al.

tential into ultra-thin carbon foils, which strip electrons to create secondary

particles. These ions then travel through a field-free TOF chamber, where their flight time is measured to determine mass-to-charge ratio (M/q). Heavier ions move more slowly, enabling species discrimination. The detection system uses microchannel plate (MCP) detectors and delay-line anodes to track the position and timing of ion impacts, correcting for path-length variations to improve mass resolution. The HPCA's electronics process events at rates up to 20 MHz, with dead-time correction to ensure counting accuracy. Calibration is achieved via the Energetic Plasma Ion Calibration (EPIC) system, which generates precise multi-species ion beams to validate energy, angle, and mass responses. This ensures the instrument's performance across its operational range, including alignment of TOF bins and verification of RF filtering efficiency. The HPCA delivers angular resolution of 11.25° azimuth x 22.5° elevation, mass resolution $(M/\Delta M)$ of 4, and full 3D velocity distributions every 10 seconds (half the spacecraft spin period). By resolving ion contributions to reconnection, the HPCA provides insights into energy conversion, plasma transport, and mass flow rates across boundaries like the Magnetopause, advancing our understanding of space plasma physics.

2.2 Spacecraft Orbit and Data Collection

MMS Orbits were changed during different phases of the mission. In the First stage, the orbit of the satellite is highly elliptical, ranging to $12r_e$, and it increases to $25r_e$ during phase 2, and during phase 3, the orbit is increased to $29r_e$ [Giles et al., 2015].

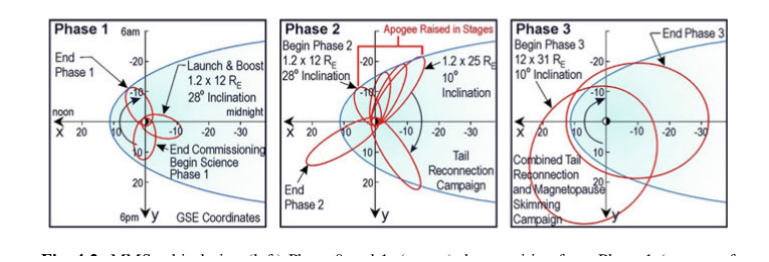


Figure 2.4: MMS Satellite Orbits During Different Phases. The orbits are in GSE coordinates in the x-y plane. (Credits: NASA/SwRI)

MMS Satellite has two operational modes (fast survey and slow survey).

For data collection, there are three types of collection: fast, slow, and burst mode [Baker et al., 2016]. Multiple categories (Figure: 2.5) of data are generated by multiple levels of calibration.

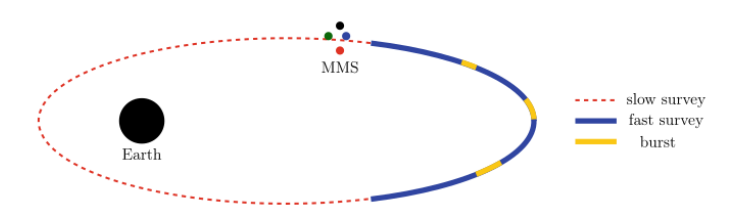


Figure 2.5: MMS satellite orbit and Region of Interest(ROI) where satellite instruments work and collect the data.

Level 1 data are fully resolved raw data, level 2 data are calibrated level 1 data, and level 3 data are generated on the basis of events. In this thesis, level 2 data is used.

2.2.1 MMS Data Levels

MMS team will manage, disseminate, and produce multiple types of data, for each level of data has some fixed level of refinements [Baker et al., 2016].

Raw Data Products

This data is collected at the ground station and ground support equipment. It contains communication artifacts and datasets that may overlap.

Level 0 Data Products

This data consists of raw, reconstructed instrument, payload, and spacecraft data, with all communication artifacts removed, such as duplicate data, synchronization frames, and communication headers. Typically, this data is stored in binary packets following the Consultative Committee for Space Data Systems (CCSDS) standard.

Level 1A Data Product

Data is de-commutated but not calibrated raw data in full resolution, time referenced, and "extracted telemetry items."

Level 1B Data Product

In this engineering calibration, the data is annotated with ancillary information such as ephemeris, attitude data, and initial instrument-level science calibration is performed.

Level 2 Data Product

This is the revised Level 1 dataset, converted into physical units and supplemented with calibrated geophysical parameters. It represents the most basic tier of research-grade scientific data and retains the original Level 1 time resolution.

Level 3 Data Product

The data have been resampled in both time and space and integrated with measurements from other MMS instruments to produce a consolidated dataset.

2.3 Wind Satellite

To verify the Magnetopause distance calculated from the MMS satellite crossing, we utilized data from the solar wind measurements of the Wind satellite. The Wind satellite, officially known as the Global Geospace Science (GGS) Wind spacecraft, is a NASA mission launched on November 1, 1994. Its primary objective is to study the solar wind and its interactions with Earth's magnetosphere.

Positioned in a halo orbit around the Sun-Earth L1 Lagrange point, Wind continuously observes the solar wind—streams of charged particles emitted by the Sun—before they reach Earth. This provides essential data for understanding space weather and its effects on satellite operations and communications. The spacecraft is spin-stabilized, weighs about 1,250 kg, and

carries a suite of scientific instruments designed to measure radio waves, plasma, energetic particles, and magnetic fields in interplanetary space.

Originally intended for a three-year mission, Wind has far exceeded its planned lifespan and, as of 2025, remains operational. It has contributed data to thousands of scientific publications and supported other solar research missions. Wind's ongoing observations are crucial for monitoring and predicting solar activity, which is vital for protecting technology and infrastructure on Earth.

2.3.1 Wind Magnetic Fields Investigation (MFI)

Working Principle

The Wind spacecraft's Magnetic Fields Investigation (MFI) utilizes dual triaxial fluxgate magnetometers to measure the interplanetary magnetic field (IMF) with high precision. These magnetometers are mounted on a 12-meter deployable boom to minimize interference from the spacecraft's own magnetic field. The outboard sensor is located at the tip of the boom, while the inboard sensor is positioned midway, enabling real-time subtraction of residual spacecraft-generated fields [Lepping et al., 1995].

Each magnetometer operates using a feedback-driven fluxgate sensor. The sensor generates a current proportional to the external magnetic field, which is then used to nullify the detected field, allowing for precise measurement. The system features:

- **Dynamic range:** Adjustable from ± 4 nT to $\pm 65,536$ nT to prevent saturation.
- **Noise performance:** Less than 0.006 nT root mean square (RMS) for signals in the 0–10 Hz range.
- **Redundancy:** Fully redundant sensors and electronics for enhanced reliability.

Sampling Rate and Data Modes

The MFI operates in several data modes to balance scientific needs and telemetry constraints [Sza]:

- 1. **Standard Mode:** Provides averaged data at **10.87 vectors per second** (vps).
- 2. **Snapshot Memory:** Captures high-resolution bursts at **44 vps** for 2.7 minutes, triggered by specific events such as sudden field changes.
- 3. **Averaged Data Products:** Includes 3-second, 1-minute, and 1-hour averages for long-term studies.

Data Handling and Calibration

Onboard processing reduces the raw 44 vps data through averaging and compression. Periodic in-flight calibrations, using internal coils, ensure measurement accuracy (with errors less than 0.08 nT). The robust design and versatile sampling capabilities of the MFI have made it a cornerstone for studying solar wind dynamics and space weather since the Wind satellite's launch in 1994.

2.3.2 Solar Wind Experiment (SWE) on Wind Spacecraft

Working Principle

The Solar Wind Experiment (SWE) on NASA's Wind spacecraft is a multisensor plasma instrument designed to measure solar wind ions and electrons. It comprises three subsystems [Ogilvie et al., 1995]:

- **Dual Faraday Cups (FC):** Measure ion fluxes using modulated electric fields (150 V to 8 kV range) to filter particles by energy/charge. Currents from collected ions are synchronously detected at 200 Hz.
- Vector Electron and Ion Spectrometer (VEIS): Uses electrostatic
 analyzers to measure 3D velocity distributions of electrons (7 V-24.8
 kV) and ions via 127° deflection in cylindrical electric fields.
- **Strahl Sensor:** Specialized toroidal analyzer for high-resolution measurements of field-aligned electron beams ("strahl") near the interplanetary magnetic field direction.

Sampling Rates and Modes

• Faraday Cups:

- Full-scan mode: 31 energy windows scanned every 93 seconds (3 s/rotation).
- Tracking mode: 14 windows scanned every 42 seconds for dynamic solar wind conditions.
- Time resolution: 3 seconds for bulk parameters (velocity, density).

• VEIS:

- Energy scans: 16 steps per analyzer every 60° spacecraft rotation.
- Electron/ion alternation: Sequential measurements with 5 ms minimum dwell time per energy step.

• Strahl Sensor:

- Angular resolution: 5° per anode.
- Time resolution: 31 ms per anode measurement.

Data Handling and Calibration

• Onboard Processing:

- Faraday Cup data compressed via logarithmic analog-to-digital conversion (10-bit dynamic range).
- VEIS pulse-counting with channeltrons and charge-sensitive preamplifiers.

• Calibration:

- UV calibrator: Monthly optical fiber-fed UV lamp checks for VEIS detector gains (±1% accuracy).
- In-flight Faraday Cup calibration: Internal coils verify sensitivity (;0.08 nT error.

• Telemetry:

- Key parameters (density, velocity, temperature) transmitted in real-time.
- Full datasets downlinked 2–3 times weekly.

Key Specifications

Parameter	Faraday Cup	VEIS
Energy/charge range	150 V–8 kV	7 V–24.8 kV
Geometric factor	1.1×10^2 cm ² sterad	4.6×10^{-4} cm ² sterad
Angular resolution	±60°	7.5°×6.5°
Dynamic range	10 ⁵	$10^3 - 10^4$

Post-Launch Modifications

- 2001: VEIS high-voltage failure led to strahl sensor repurposing for primary electron measurements.
- Current operations: Combined strahl/Faraday Cup data used for electron temperature anisotropy studies.

Chapter 3

Observation and Data Analysis

I'm attempting to observe the Earth's Magnetopause using MMS satellite data during periods of extreme solar wind interactions, cme storms, and non-storms. S. E. Haaland et al. proposed methods for cluster missions to determine Magnetopause location, Magnetopause shifting velocity during events, and Magnetopause width. It is crucial to determine the precise Magnetopause location during the spacecraft's crossing of the Magnetopause.

3.1 Minimum Variance Analysis

This approach requires time series data that includes structures that the spacecraft crosses, such as current layer crossings or Magnetopause crossings. Therefore, the field component must be continuous along a preferred direction associated with the normal to a wave front or normal to an idealized boundary for the magnetic field to be divergence-free. Accordingly, minimizing the magnetic field's variance concerning a direction x will yield a k direction, and the stationary structure is described by the main direction in the variance (Dunlop et al. [1995]). For a given direction x, the magnetic field variance is expressed as

$$\sigma^2 = \frac{1}{N} \sum_{n=1}^{N} |(B_n - \langle B \rangle) \cdot \hat{n}|^2$$

This MVA method for magnetic field comprises estimating the normal direction of the structure and the direction where the variance is minimised.

By using Lagrange multiplier λ , solve a set of equations we have

$$\sum_{\nu=1}^{3} M_{\mu\nu}^{B} n_{\nu} = \lambda n_{\nu}$$

 $\mu = 1, 2, 3, v = 1, 2, 3$ represents x,y,z directions(GSE) and M is

$$M_{\mu
u}^{B}n_{
u}=\left\langle B_{\mu}B_{
u}
ight
angle -\left\langle B_{\mu}
ight
angle \left\langle B_{
u}
ight
angle$$

Finding eigenvalues and matching eigenvectors of $M_{\mu\nu}^B n_{\nu}$ (Grönlund [2021]) is the next step in determining the normal direction. The normal direction is represented by the eigenvector that has the lowest eigenvalue. When magnetic field components are multiplied by this eigenvector, structure crossing—in our example, the Magnetopause crossing—is plainly visible due to the projection of magnetic field components in the direction of normal.

3.2 Detection of the Magnetopause

Our study focuses on detecting the Magnetopause by conducting an analysis without relying on any pre-developed software or algorithms. Instead, we developed a semi-automated Python pipeline that identifies fluctuations and Earth's Magnetopause crossings using data from MMS satellites. Each year, from October to July, the satellites traverse the X-Y plane (GSE) of the Magnetopause. To facilitate data handling, we created a Bash script that downloads all satellite data and organizes it into corresponding folders. For our analysis, we utilize data from two satellite instruments: FPI and FGM.

The pipeline requires an input file in '.txt' format containing the following information: the start date for Magnetopause detection (e.g., 20221023060000), the number of Magnetopause crossings, the path to the folder containing FPI data, the path to the folder containing FGM data, the path to the folder where output plots (FPI and FGM) should be saved, a CSV file with timestamps of Magnetopause crossings along with satellite names (e.g., mms1, mms2), and the name of this CSV file. Each input must be provided on a separate line in the .txt file and must follow a specific sequence. The output CSV file generated by the pipeline contains crossing times as well as fluctuation timestamps. To ensure accuracy, we manually review the output plots (FPI

and FGM) to select the correct timestamp for one satellite. The pipeline then automatically determines corresponding timestamps for other satellites based on this selection.

Working of the Pipeline

The pipeline begins by extracting file paths for FPI and FGM data based on the input date. For FPI (which operates in fast mode and stores 2-hour intervals per file), it collects paths for the next 14 hours (spanning seven files). For FGM (which provides daily data), it retrieves the path for the full day. The system is designed to ensure Magnetopause crossings fall within this 14-hour FPI-FGM data window.

To detect crossings, two functions are implemented

- Magnetic Field Fluctuation Detection: Identifies changes in the magnetic field.
- Energy Spectra Change Detection: Analyzes shifts in plasma energy spectra, offering higher accuracy than the first method.

The pipeline automatically verifies that detected crossings align with the 14-hour data range, ensuring consistency between FPI and FGM observations.

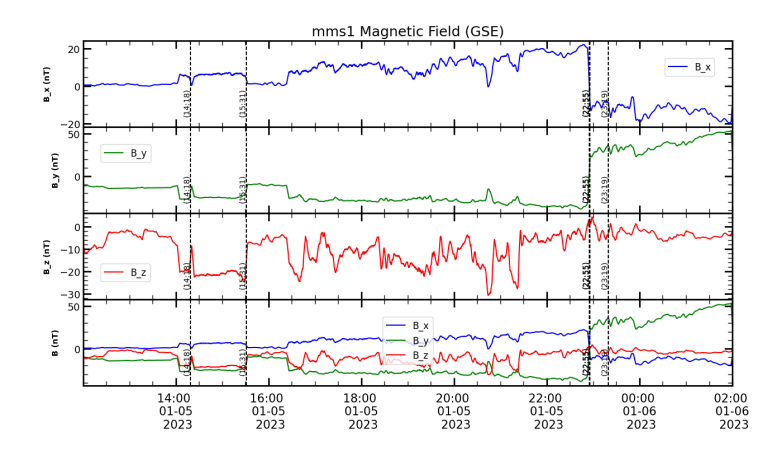


Figure 3.1: Magnetic Field Components are shown, the vertical line that detects the fluctuation in the data

The detected fluctuations are marked by dashed vertical lines in Figures 3.1 and 3.2. A distinct change in the plasma energy spectrum is visible at

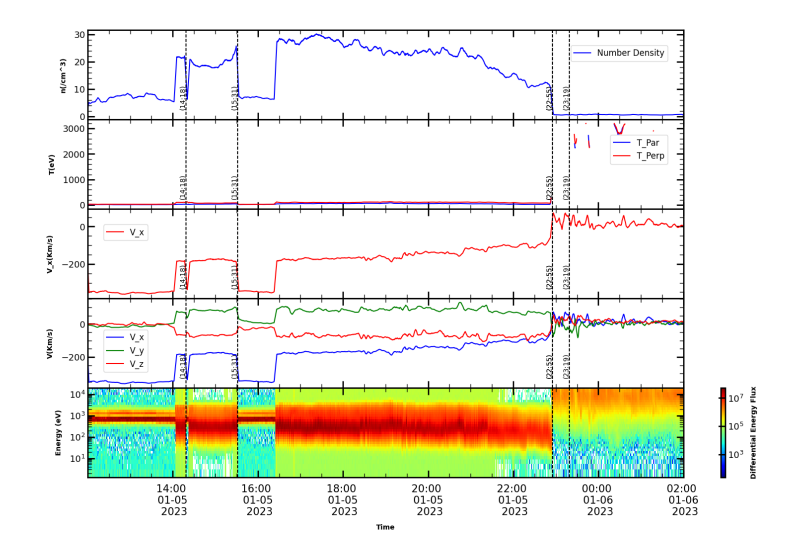


Figure 3.2: Data of the FPI Instrument are shown, plasma parameters and vertical lines with the fluctuation detected by the algorithm.

22:55, which corresponds to the Magnetopause crossing. This timestamp must be manually selected as a Magnetopause crossing timestamp. When this is run with the Ubuntu terminal, it also takes additional hours to add because of the trajectory of the satellite, we have to add some additional hours so that it can take write paths of fpi instrument data, as well as fgm instrument data.

3.3 Magnetopause Model

Various models have been made for the size and shape of the Magnetopause in the past. These models use the inverse trigonometric function to describe the Magnetopause(Roelof and Sibeck [1993]). Some other models use a general equation of an ellipsoid with two parameters or a quadratic equation. The model was generated with the data of satellite the satellites ISEE 1 and 2, Goes 2,5, and 6, IMP 8, and ISEE 3.

In my analysis, I utilized the empirical model developed by Shue et al. (1997) to characterize the size and shape of Earth's Magnetopause in response to varying solar wind conditions. This model introduced a novel functional form that is both simple and flexible, capturing the flaring of the magnetotail and the compression of the dayside Magnetosphere due to solar wind dynamic pressure and the orientation of the interplanetary magnetic

field (IMF), particularly the Bz component.

The model defines the radial distance to the Magnetopause, r, as a function of the angle θ between the Earth-Sun line and the direction of interest, using the formula(Shue et al. [1997]):

$$r(\theta) = r_0 \left(\frac{2}{1 + \cos \theta}\right)^{\alpha}$$

Here, r_0 represents the subsolar standoff distance, and α quantifies the level of tail flaring. These parameters are dynamically adjusted based on the solar wind dynamic pressure D_p and IMF B_z through empirically derived relations:

For r_0 , a power-law dependence on D_p and a piecewise linear relation with B_z were established:

$$r_0 = \begin{cases} (11.4 + 0.013B_z) \cdot D_p^{-1/6.6}, & B_z \ge 0\\ (11.4 + 0.14B_z) \cdot D_p^{-1/6.6}, & B_z < 0 \end{cases}$$

For α , a linear dependence on both B_z and D_p was proposed:

$$\alpha = (0.58 - 0.010B_z)(1 + 0.010D_p)$$

These formulations were derived from an extensive dataset of 553 Magnetopause crossings recorded by satellites such as ISEE 1/2, AMPTE/IRM, and IMP 8, with solar wind parameters provided by IMP 8 and ISEE 3. The model's strength lies in its ability to provide an explicit and continuous representation of the Magnetopause under a wide range of solar wind conditions, with direct applications in space weather prediction and operational planning for geosynchronous satellites.

Chapter 4

Results and Discussion

The Earth's Magnetopause and how its boundary behaves during various solar storm and non-storm periods are the primary subjects of this study. The Magnetopause is the area where Earth's magnetic field and IMF are balanced within magnetosphere. The Magnetopause shifts toward Earth when the IMF is high, and its size increases when the IMF is low. This study shows how much the Magnetopause shifts in comparison to a non-storm day.

4.1 Magnetopause Identification

More information about the use of MMS satellite data in this study can be found in chapter (2). for identifying the Magnetopause magnetic field data of mms fluxgate magnetometer data (FGM), which has a sampling rate of 128 samples per second and an accuracy of 0.1nT. Additionally, this system's center is assumed to be in Earth's center, and magnetic field is displayed in geocentric solar ecliptic coordinates, with positive x direction points sunward and positive z points northward and also the change in energy spectrum of Ions changes significantly because Magnetopause separetion boundary between the two plasma so the magnetospheric plasma have less energy compar. The spacecraft entered the Magnetopause when the magnetic B_z component turned negative (southward). Time was calculated at that location, and the spacecraft's location in GSE coordinates was determined after the initial reversal of the B_z component, and the Magnetopause

topause location was determined by calculating the radial distance of the spacecraft. The all plots that are shown is after the smoothing of data with the method of box-car smoothing.

4.1.1 Non Storm Day Magnetopause

This event occurs when the mms satellite crosses the Magnetopause on May 4, 2024. The plot below shows the IMF being observed first, followed by the beginning of the Magnetosheath observation. On this day, data and during this time, DST Index is greater than -20nT(provided by Omni web Nasa), so it is considered a nonstorm day. There was a geomagnetic storm on May

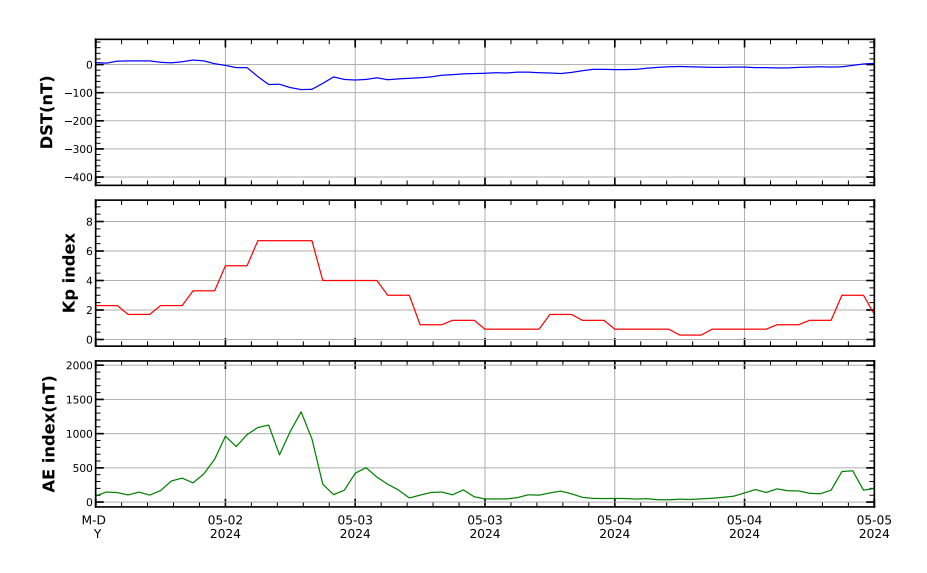


Figure 4.1: The Figure shows Dst, Kp, and AE Index Variation of four Days. Starting from 2 May to 5 May 2024

2, as shown by increased Kp and AE index values and a decrease in the Dst index in Figure 4.1. On May 3, the indices indicate the recovery phase of the storm. By our observation day on May 4, the Kp index was less than 2, the AE index was below 100 nT, and the Dst value was greater than - 50 nT. These values show that May 4 was a quiet day with no significant geomagnetic activity.

The figure 4.2 shows three important events related to Earth's magnetic environment. The first blue vertical dashed line marks the beginning of the Magnetosheath, which is the region where fluctuations in the magnetic field start. This area lies between the solar wind and Earth's magnetic field and

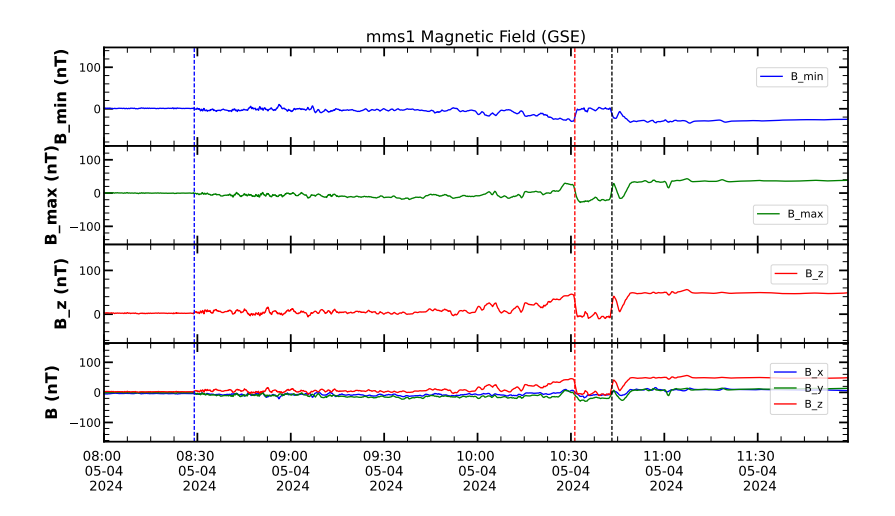


Figure 4.2: MMS1 Fluxgate magnetometer data of Magnetic field First two figures are the magnetic field component in the direction of minimum and maximum variance direction, and the last plot includes the magnetic field X, Y, Z components in GSE coordinate and time in UTC format.

contains disturbed solar wind particles. The red dashed line at 10:30 indicates the crossing of a current sheet. This is seen as a sudden change in the magnetic field and represents a thin layer where electric currents flow. Current sheets are important because they often occur during magnetic reconnection. The last green vertical line shows the Magnetopause crossing, which is the boundary. At 10:43, the magnetic field reverses clearly, signaling that the satellite has crossed this boundary. At this time, the satellite is located 11.63 Earth radii (Re) from Earth. Using the angle of 35.5° between the satellite's position and the Earth-Sun line, the Magnetopause nose distance (the closest point of the Magnetopause toward the Sun) is calculated to be 11.08 Re, based on the model by [Shue et al., 1997].

The light blue curve in Figure 4.3 represents the spacecraft's orbit, while the dashed shape indicates the expected position of the Magnetopause at 10Re under typical solar wind conditions. The dark blue shape shows the Magnetopause location as calculated by the model. At the time of the crossing, the Bz component of the magnetic field was positive, with a value of 46 nT, which caused the Magnetopause boundary to shift Earthward. This extension measured approximately 1.08Re.

The MMS Fast Plasma Investigation (FPI) measures important proper-

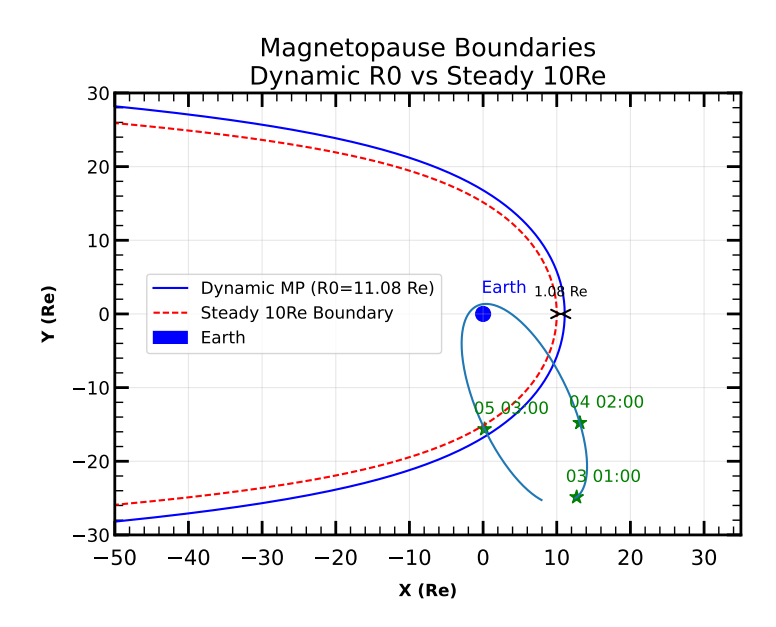


Figure 4.3: Spacecraft orbit in X-Y plane In GSE, the calculated Magnetopause and spacecraft location at different times are shown. The red star in orbit is the SC location at the time of crossing.

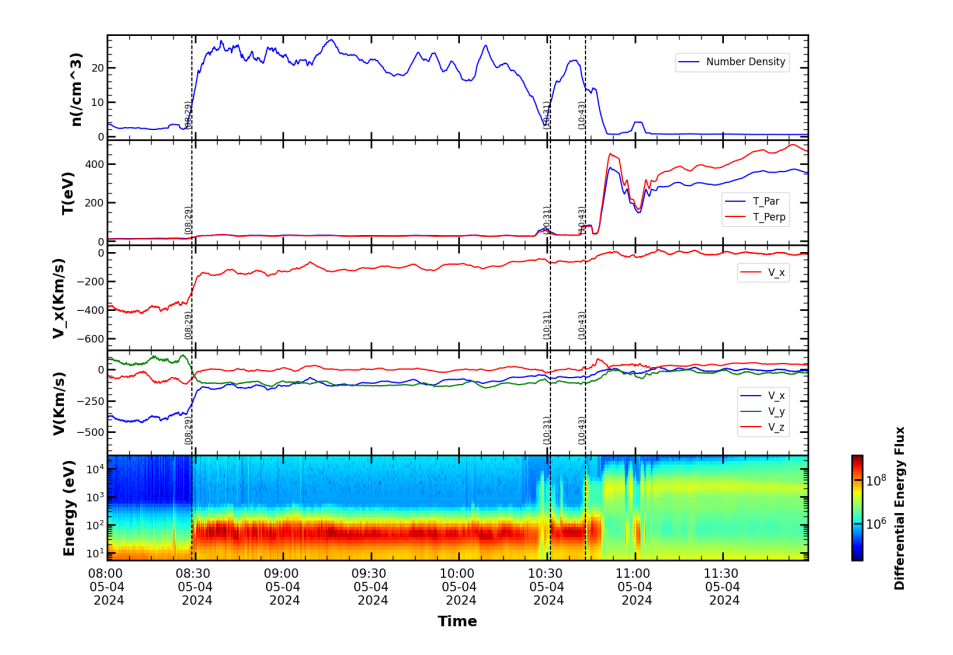


Figure 4.4: MMS1 FPI Instrument Measurement number density of Ions Temperature Velocity Vectors and Energy spectrum. The vertical dashed line indicates the starting of the Magnetosheath, current sheet, and Magnetopause crossing(left-to-right lines) and the time shown in UTC formate.

ties of space plasma, such as electron density, electron temperature (both across and along the magnetic field), and velocity, every 30 milliseconds as

it crosses the Magnetopause (MP). When the solar wind reaches Earth from the Sun, the electrons slow down and build up near the Magnetopause, creating a thin current sheet. This effect can be seen in Figure 4.4 around 10:31 UTC, where both the number of electrons and their energy increase.

After the spacecraft moves past the Magnetopause, the number of particles drops while their temperature rises. At the moment of crossing, the number of ions is about 1 particle per cubic centimeter, which makes sense because the plasma is deflected at the Magnetopause, so fewer particles are detected.

The electrons, or charged particles, lose some of their energy as they approach the Magnetopause. Their velocity in the x-direction (toward or away from the Sun) hovers around zero, and the other velocity directions are also close to zero. These changes are clear signs that the spacecraft has crossed the Magnetopause. In Figure 4.4, you can see the electron number density go up at the start of the Magnetopause due to the buildup of electrons in that region.

4.1.2 Storm Day Magnetopause

At the beginning of May, the number of sunspots facing Earth was 5, with a total sunspot area of 40 millionths of a solar hemisphere (MH). Both the number and area of sunspots increased, peaking on May 9. On this day, the sunspot number rose to 81, and the area expanded to 1090 MH. Interestingly, while the sunspot number decreased to 58 the following day, the total area continued to grow, reaching 2400 MH, indicating that the existing sunspots became significantly larger see Table 4.1.

Multiple coronal mass ejections (CMEs) and solar flares were observed from active region AR13664 on May 8–9, 2024 [Hayakawa et al., 2024]. As a result of these combined CMEs impacting Earth, intense auroras were seen at unusually low latitudes, far beyond their typical appearance in the polar regions. This led to a G5-class geomagnetic storm on May 10–11, popularly referred to as the "Mother's Day Storm."On May 11, there are 19 coronal mass Ejections observed between 5-15 May, and in this there are 12 Halo CMEs are observed by LASCO. The list of Halo CMEs can be seen in the Table 4.2 During this period, multiple solar flares were observed, including

Table 4.1: Daily sunspot numbers and their corresponding sizes (in MH) for May 2024 Storm(credit to NOAA SWPC

Date	Number of Sunspots	Size (MH)
2024/05/01	5	40
2024/05/02	13	120
2024/05/03	16	240
2024/05/04	20	310
2024/05/05	20	580
2024/05/06	22	560
2024/05/07	37	630
2024/05/08	62	1200
2024/05/09	81	1090
2024/05/10	58	2400
2024/05/11	43	2100
2024/05/12	28	1920
2024/05/13	15	1170
2024/05/14	15	1170

Table 4.2: Halo CMEs: Date, Time, Angular Width, and Speed Between 5-15 May 2024. These CMEs' Information is taken by LASCO.

Date	Time [UT]	Angular Width (°)	Linear Speed (km/s)
2024/05/08	05:36:06	360	530
2024/05/08	22:24:05	360	952
2024/05/09	09:24:05	360	1280
2024/05/09	18:52:00	360	1024
2024/05/10	07:12:05	360	953
2024/05/11	01:36:05	360	1614
2024/05/12	01:48:05	360	454
2024/05/13	08:48:06	360	1690
2024/05/14	17:00:05	360	2010
2024/05/14	17:48:05	360	1407
2024/05/15	08:36:07	360	1648
2024/05/15	20:56:53	360	1250

several of high intensity. Notably, an X3.38-class flare occurred on 9 May 2024 at 13:14 UT, followed by an even stronger X3.9-class flare on 10 May 2024 at 06:54 UT. In Figure 4.5, a coronal mass ejection (CME) associated with activity from 7–8 May 2024 is shown. These images were captured using the LASCO (Large Angle and Spectrometric Coronagraph) coronagraphs C2 and C3, aboard the SOHO spacecraft. LASCO C2 observes the corona from approximately 1.5 to 6 solar radii, while C3 extends this range to about 30 solar radii. Both coronagraphs utilize white-light filters to block direct sunlight and enable detailed imaging of the outer solar atmosphere, helping visualize CME structures as they propagate through the corona.

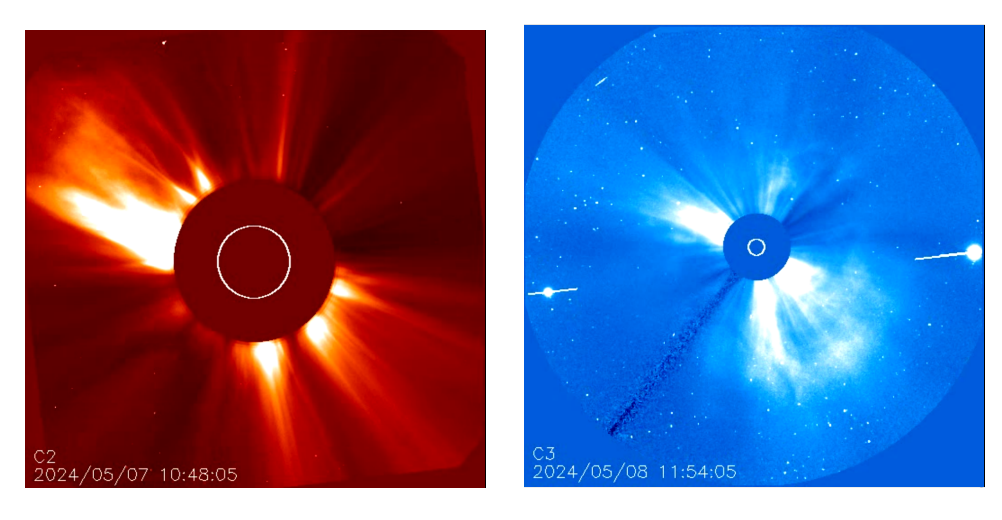


Figure 4.5: Coronal Mass Ejection occurred on May 7-8 are shown, Images from LASCO C2 and C3 Filters

A comprehensive Magnetopause study was carried out during this period, with the geomagnetic storm being detected by the Magnetospheric Multiscale (MMS) mission. Since the MMS spacecraft was positioned near the Magnetopause at the time, it provided a unique opportunity to analyze in situ plasma and magnetic field data with high temporal resolution. The storm was marked by a significant drop in the Disturbance Storm Time (Dst) index, which reached a minimum of –412 nT on May 11. The Dst index measures the intensity of the ring current around Earth and is commonly used to quantify the strength of geomagnetic storms. Furthermore, the Interplanetary Magnetic Field (IMF) reached a peak magnitude of 73 nT, indicating a strong coupling between the solar wind and Earth's magnetosphere.

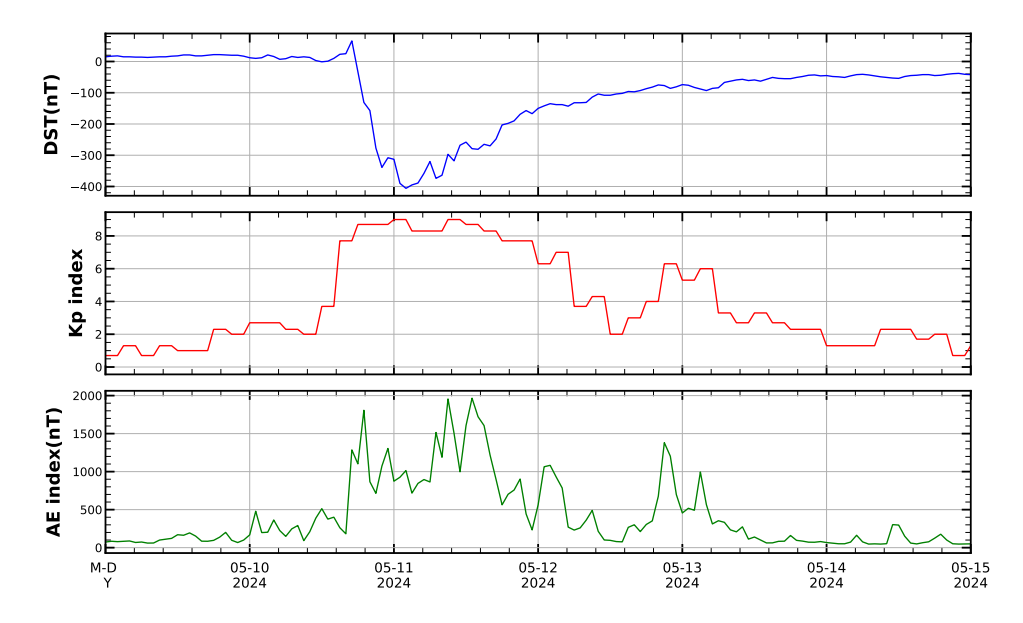


Figure 4.6: The variation of DST, Kp, and AE Index is shown on 11-May, starting from 9-15 May 2024

The Kp index, which measures global geomagnetic activity on a scale from 0 to 9, reached its maximum possible value of 9, signifying an extreme geomagnetic disturbance. Variations in the Auroral Electrojet (AE) index—shown in Figure:4.6 further indicate enhanced auroral activity and increased ionospheric currents during the event. This geomagnetic storm is considered the most intense since the 2003 Halloween storm, which had a Dst minimum of –422 nT [Lazzús and Salfate, 2024, Pierrard et al., 2024].

Figure: 4.7 As seen in the plot, the magnetic field Bz component reverses after 12:27, which is considered the current sheet starting, and at last, there is a Magnetopause crossing detected. The solar storm's magnetic field strength can reach up to 70 nT during this event. The MP shifts toward Earth as a result of this high IMF value.

In the figure:4.7, the blue vertical line is the start of the Magnetosheath, followed by the current sheet crossing the red vertical line, and lastly green line is the final Magnetopause crossing with the z component turning towards northward. The Magnetopause crossing is shown in Figure:4.7 at 14:46. At that point, the spacecraft X, Y, and Z components (GSE) are 5.99Re,-2.87Re, and -0.005Re, and the radial distance is determined to be 6.65Re, and the calculated Magnetopause distance with the model is 6.48Re.

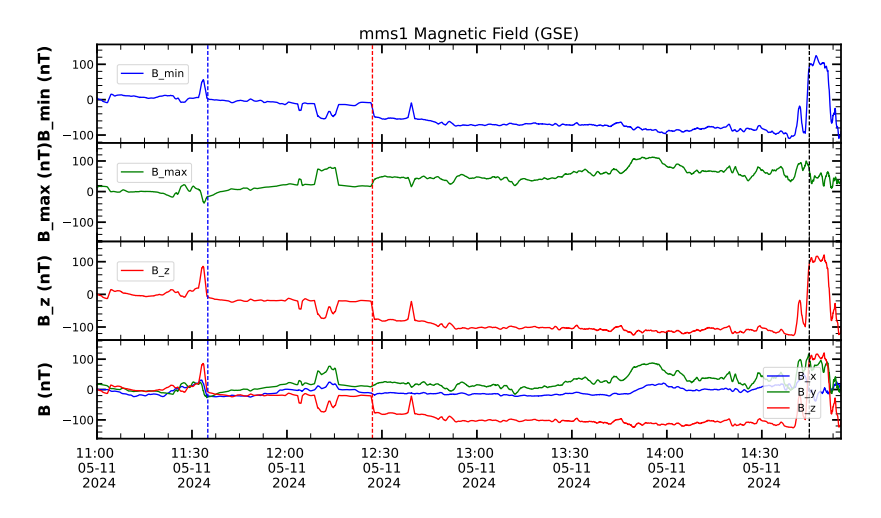


Figure 4.7: MMS1 Fluxgate magnetometer data of Magnetic field First two figures are the magnetic field component in the direction of minimum and maximum variance direction and the last plot includes the magnetic field X, Y, Z components in GSE coordinate and time in UTC format.

In the Figure: 4.8 at 12:27, there is an increase in the number density and temperature, which is the signature of the current sheet and when the number density decreases at 14:49, there is a decrease in the current density as well as in the temperature, which is the Magnetopause crossing detected by the algorithm and also the energy spectrum shows change in at the time of crossing. All of these characteristics are also indicative of MP. Since this is a stormy period, there are several fluctuations before the MP crossing is seen.

Two Magnetopause boundaries are shown in the provided Figure 4.8, one during a storm and another is the standoff distance of MP. Compared to this, the compression of the Magnetopause detected is 3.51Re towards Earth. This observation is almost in the ecliptic plane because the z component of the satellite is approximately +35 km, which means it is just 35km above the ecliptic plane, which is not much. The blue orbit is the spacecraft's orbit annotation, which can be seen in the figure at different times, Figure: 4.9.

A negative IMF Bz value causes the Magnetopause to shift towards the Earth, while a positive IMF Bz value results in an extended Magnetopause towards the Sun [Kumar and Pulkkinen, 2025]. These effects were observed

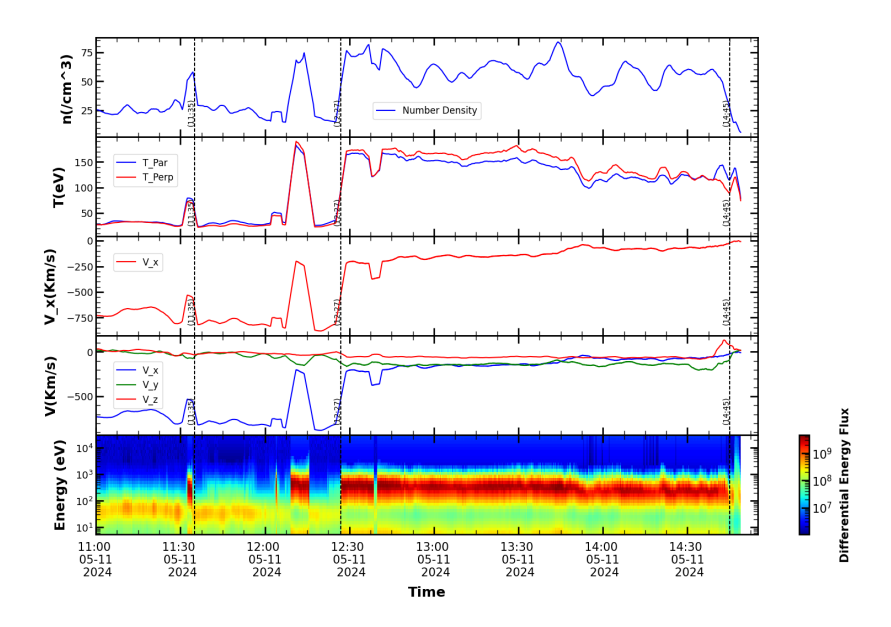


Figure 4.8: MMS fpi measurements of number density of electron, temperature of electron parallel and perpendicular to magnetic field, velocity X component and velocity X, Y, Z components(all quantities are in GSE) and energy spectrum.

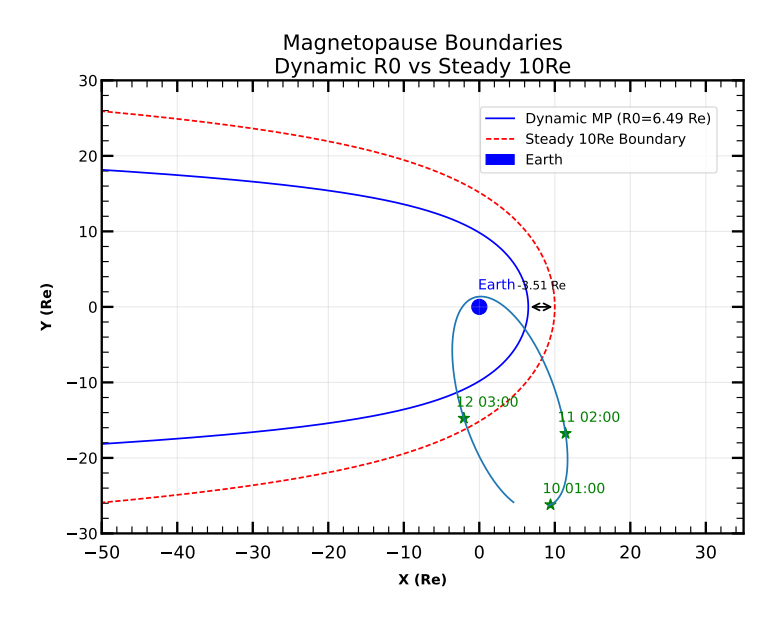


Figure 4.9: The Magnetopause compression shown during the storm comparison to the standoff distance (10Re), the compression is 3.51 Re. The light blue is the orbit of the satellite, and stars show the satellite's position at different timestamps and time in UTC format.

on the storm day (11 May 2024) and the non-storm day (04 May 2024). To study the correlation with solar wind parameters, we used data from the Wind satellite and calculated the average IMF Bz value 1.5 hours before the

Table 4.3: MP location, MP Difference, which is calculated based on the standoff distance of the Magnetopause and spacecraft location during MP crossing location.

	NonStorm Day MP	StormDay MP
MP location	11.08 Re	6.48 Re
MP Difference	+1.08 Re	-3.52 Re
S/C Location	(9.48Re,-6.58Re,-1.43Re)	(5.99Re,-2.87Re,-0.005Re)

Magnetopause crossing. The resulting IMF Bz value was approximately -21 nT.

4.2 Structure of the Earth Magnetopause

We analyzed three years of data from the MMS (Magnetospheric Multiscale) satellite mission. For each year, from October to the following July, the MMS spacecraft consistently traversed the X–Y plane of the Earth's Magnetopause. This recurring orbital pattern provides a valuable opportunity to examine the structure of the Magnetopause (MP) in detail, as well as to study its interaction with the solar wind.

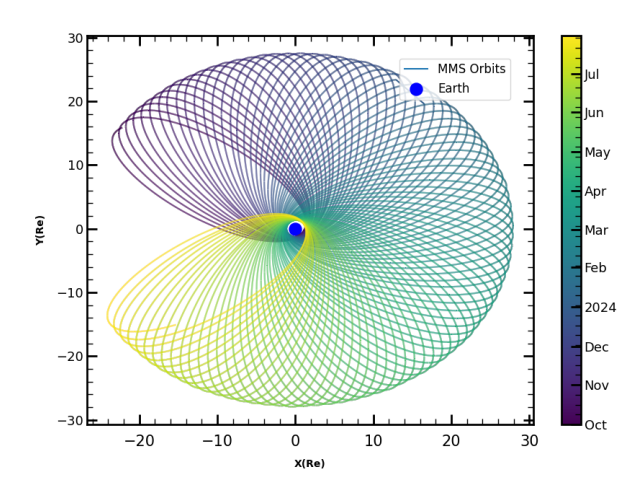


Figure 4.10: Plot of MMS1 Satellite orbit data of 10 months shows that the satellite covers the X-Y plane

Figure: 4.10 shows the orbit data of 10 Months starting from 2023-October to July-2024. During these 10-month periods each year, we identified multiple Magnetopause crossings using a custom-built detection pipeline. This

pipeline was specifically designed to analyze high-resolution MMS data and detect the distinct boundary signatures characteristic of MP crossings, such as abrupt changes in magnetic field, plasma density, and ion/electron velocity distributions. This regular and extended coverage of the X–Y plane not only allows us to resolve spatial and temporal variations in the Magnetopause structure.

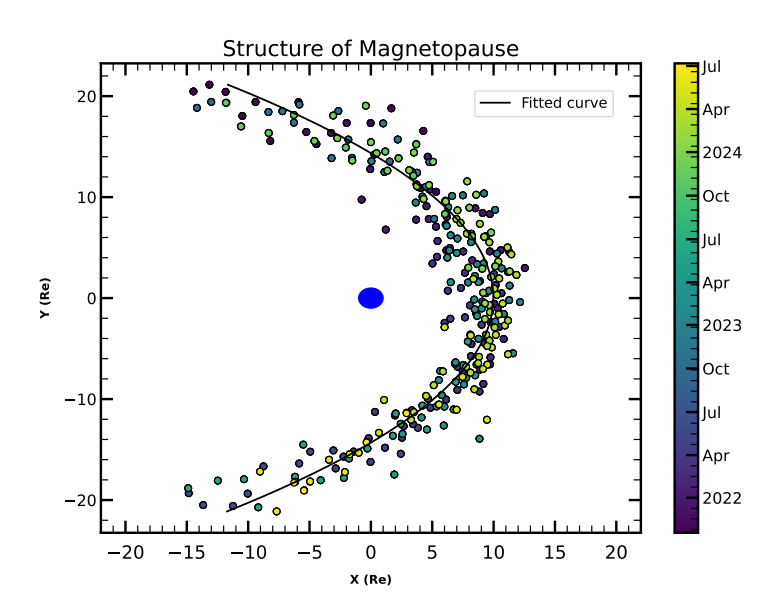


Figure 4.11: Each Point shows a Magnetopause crossing, and the corresponding color shows the time of that crossing, which is shown on the colorbar.

A total of 297 Magnetopause crossings have been identified using data from one MMS satellite, with each point incorporating observations from all four MMS spacecraft. These include both inbound and outbound crossings, as illustrated in Figure 4.11. The scatter in the data points arises due to variations in solar wind dynamic pressure. The blue dot denotes Earth, scaled to one Earth radius ($1R_E$), while the black curve represents a fitted quadratic function. The goodness of fit is quantified by an R^2 value of 84.3%. The fitted curve is described by the parabolic equation:

$$X = aY^2 + bY + c$$

The resulting fit yields the equation:

$$X = -7.6 \times 10^{-6} Y^2 + 2.06 \times 10^{-3} Y + 63550$$

Here, the constant term c = 63550 km (approximately 9.97 R_E) corresponds to the radial distance of the Magnetopause nose, indicating a positional shift in the boundary.

4.3 Plasma Parameters Values

We have taken the plasma parameter values at the time of crossing to see the variation in the plasma values near the Magnetopause.

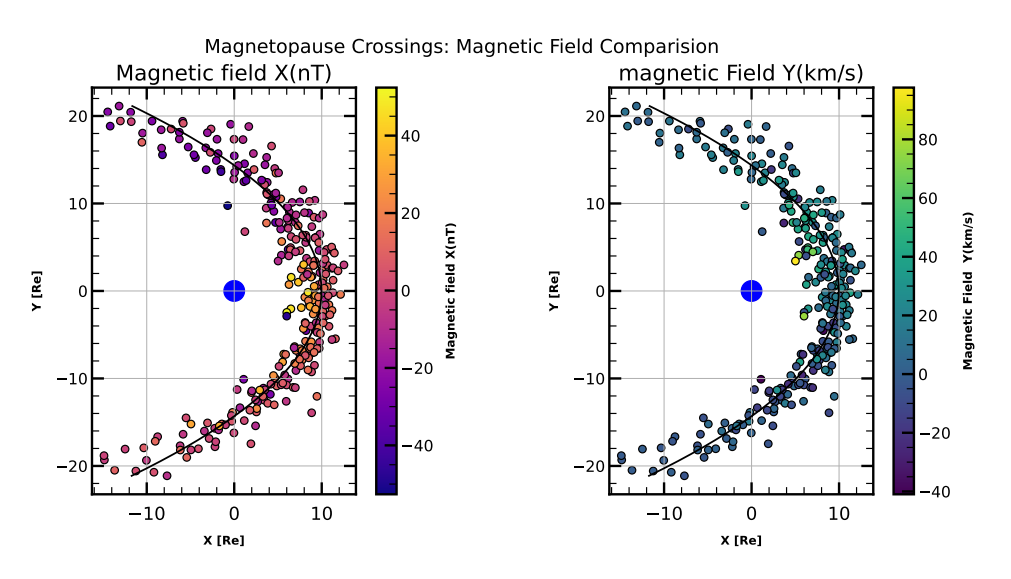


Figure 4.12: Scattered points are in the location of Magnetopause crossings and color represents the intensity of the Magnetic field. The left plot is for the magnetic field x component, and the right one is for the y component of the magnetic field.

Figure 4.12 illustrates the spatial variation of the magnetic field components at the Magnetopause crossing location. The color of the points represents the magnitude of the magnetic field measured by the MMS1 Fluxgate Magnetometer. The left plot corresponds to the X-component of the magnetic field, while the right plot represents the Y-component.

In the subsolar region, many of the points have colors close to those near zero on the colorbar, indicating that the magnetic field components are either very small or close to zero in these areas. This behavior aligns with the physics at the Magnetopause, where the magnetic pressure from Earth's field balances the dynamic pressure of the incoming solar wind. This balance results in a reduction or reversal of the magnetic field strength, particularly in the components parallel to the boundary surface.

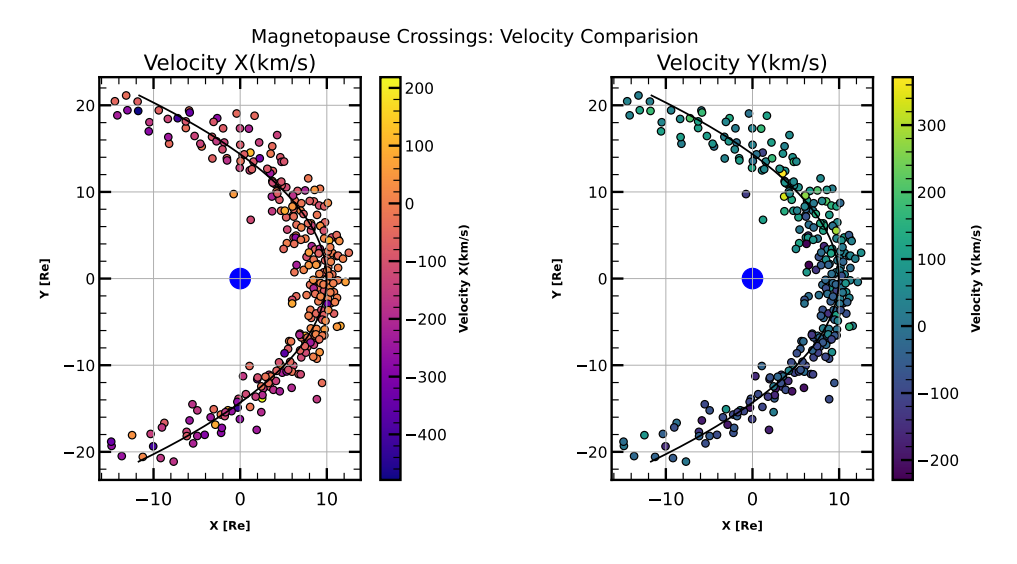


Figure 4.13: Scatter point locations are in the crossing coordinates location, and color represents the magnitude of the velocity x(left) and y(right) component

In Figure 4.13, the color of the scatter points represents the magnitude of the plasma velocity in the X and Y directions. Near the subsolar region, the scatter points show colors corresponding to values near zero on the color bar, indicating low velocity magnitudes. As we move away from the subsolar region, the velocity magnitudes increase due to the deflection of plasma flow after interacting with the Magnetopause (MP). This effect is more prominent in the Y-component of velocity compared to the X-component, since the X-direction lies along the Earth-Sun line, where flow slows as it encounters the MP. On the other hand, the Y-component experiences stronger variations due to the lateral deflection of plasma around the Magnetopause.

The figure displays the ion temperature values as measured by the FPI (Fast Plasma Investigation) instrument onboard the MMS1 spacecraft. As the spacecraft approaches the Magnetopause, ions are observed to lose kinetic energy due to the deceleration of plasma flow near this boundary. This reduction in kinetic energy directly affects the measured ion temperature, since the thermal temperature is closely related to the average kinetic energy of the particles in a plasma.

This behavior is evident in Figure 4.14, where a noticeable drop or variation in ion temperature is seen near the Magnetopause crossing. The slowdown of ions is a result of the interaction between the Magnetosheath plasma and the magnetic barrier at the Magnetopause, where plasma dy-

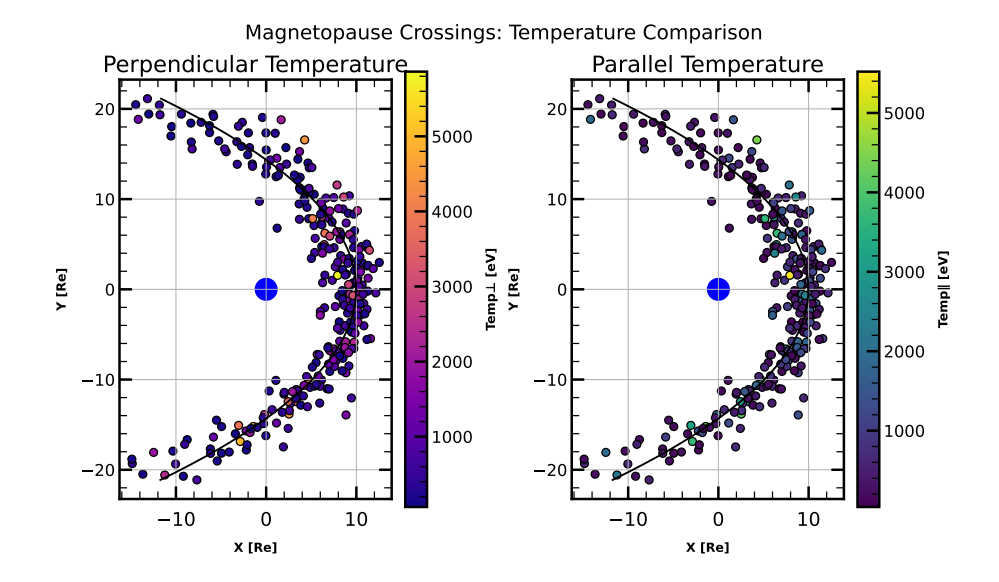


Figure 4.14: Temperature of the Ions perpendicular and parallel to the magnetic field is shown at the time and location of the Magnetopause crossing.

namics are influenced by pressure gradients, magnetic tension, and possible reconnection effects.

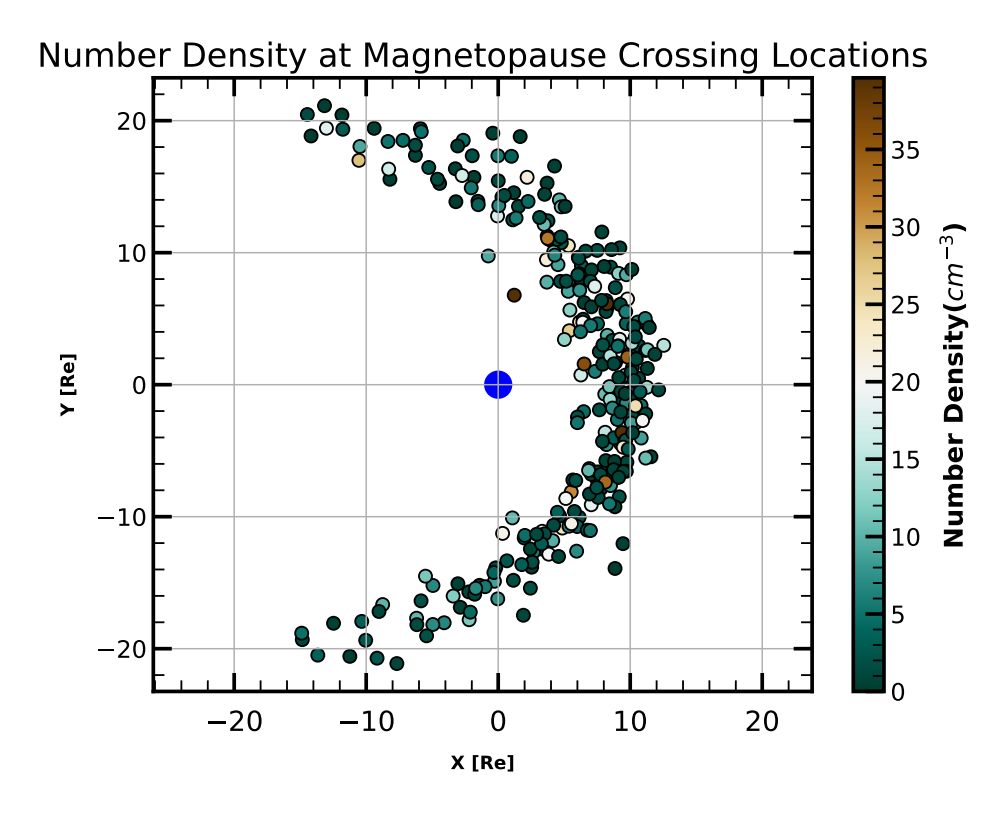


Figure 4.15: The number Density of the Ions shown at the time and location of crossing

The ion number density at the time and location of the Magnetopause

crossing is shown to be nearly zero. This is evident from the color of the scatter point, which corresponds to the near-zero values on the colorbar. The low density suggests that most of the ions are being deflected around the Magnetopause rather than crossing it directly, indicating a strong boundary and limited particle penetration.

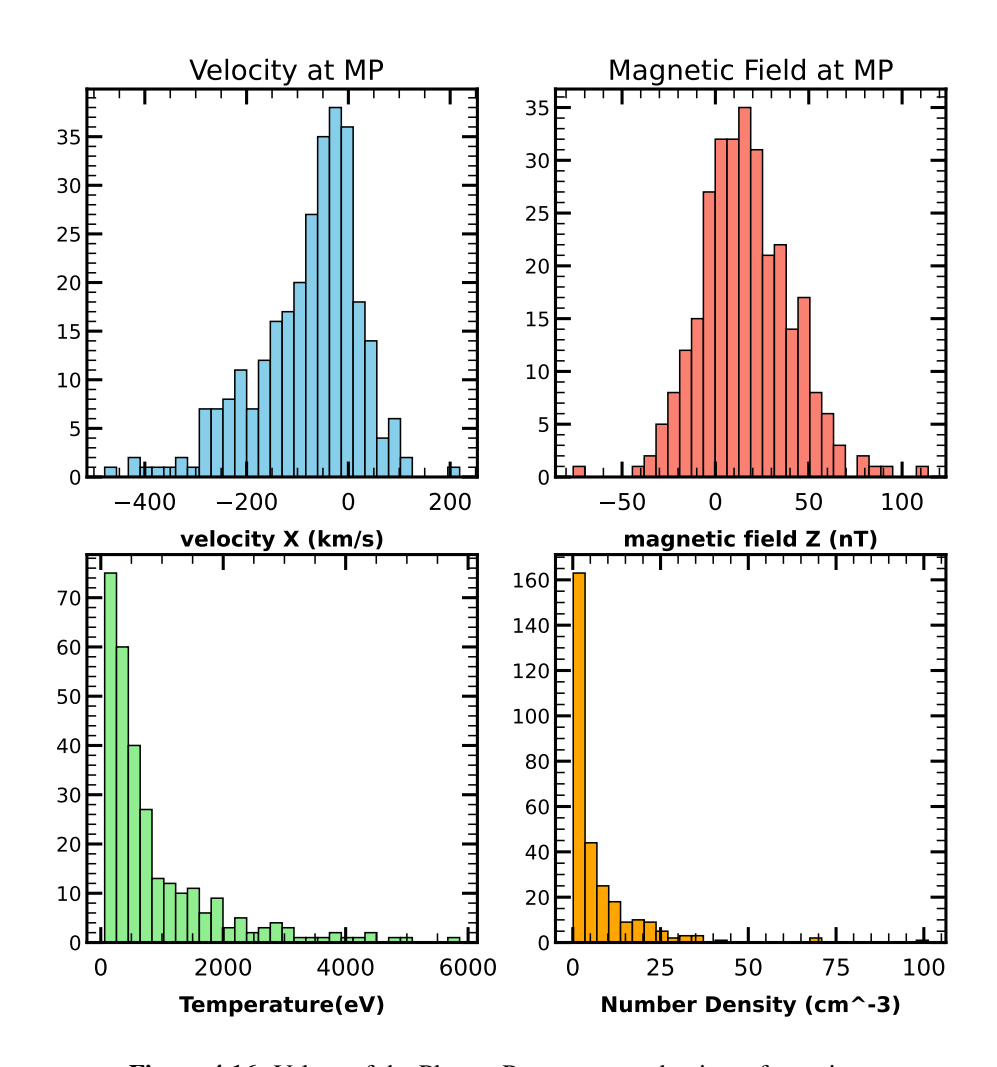


Figure 4.16: Values of the Plasma Parameters at the time of crossings

These Figures:4.16 present statistical distributions of key plasma parameters, velocity, magnetic field, temperature, and number density, measured during Magnetopause crossings. The histograms show that, at the Magnetopause, there is a wide range of observed velocities (from about -400 km/s to 200 km/s), with most values clustering near zero, indicating the transition from the relatively stagnant magnetospheric plasma to the faster-flowing Magnetosheath plasma. The magnetic field strength, shown in nanotesla

(nT), is centered around zero but spans from about -50 nT to 100 nT, reflecting the magnetic shear and rotation typical at the boundary. Temperature distributions are strongly peaked at low values (below 1000 eV), but with a tail extending up to 6000 eV, illustrating the sharp temperature gradient between the hot magnetosphere and cooler Magnetosheath. Number density is similarly peaked at low values (under $10 \ cm^{-3}$), but extends up to $100 \ cm^{-3}$, capturing the abrupt density increase as the spacecraft crosses from the low-density magnetosphere into the denser Magnetosheath. Together, these distributions highlight the sharp and dynamic changes in plasma properties that define the Magnetopause boundary and are consistent with the expected signatures of Magnetopause crossings in space physics

4.4 Magnetopause Crossing Validation

To validate the 297 Magnetopause crossings detected by the MMS satellite, we used solar wind data from the Wind spacecraft, which is positioned near Earth's L1 Lagrange point (approximately 1.5 million km sunward of Earth). Since solar wind parameters measured at L1 take time to reach Earth, a 1.5-hour average delay was applied to Wind's measurements of solar wind velocity, number density, and magnetic field components. This delay accounts for the travel time of the solar wind from L1 to Earth's Magnetopause, which was calculated using the measured solar wind speeds (typically 400 km/s).

The time-adjusted data were then input into the Shue98 empirical model (Chapter 3), which predicts the Magnetopause's subsolar distance (the nose distance from Earth's center) based on solar wind dynamic pressure and interplanetary magnetic field (IMF) conditions. By comparing the Shue98 predictions with the actual MMS satellite observations of Magnetopause crossings, we were able to assess the model's accuracy under real solar wind conditions.

The histogram displays a roughly bell-shaped distribution centered near zero, indicating that most Magnetopause crossings occur within $\pm 1 \mathrm{Re}$ of the model prediction. This suggests that while the Shue model provides reasonable approximations, there are still noticeable deviations between the

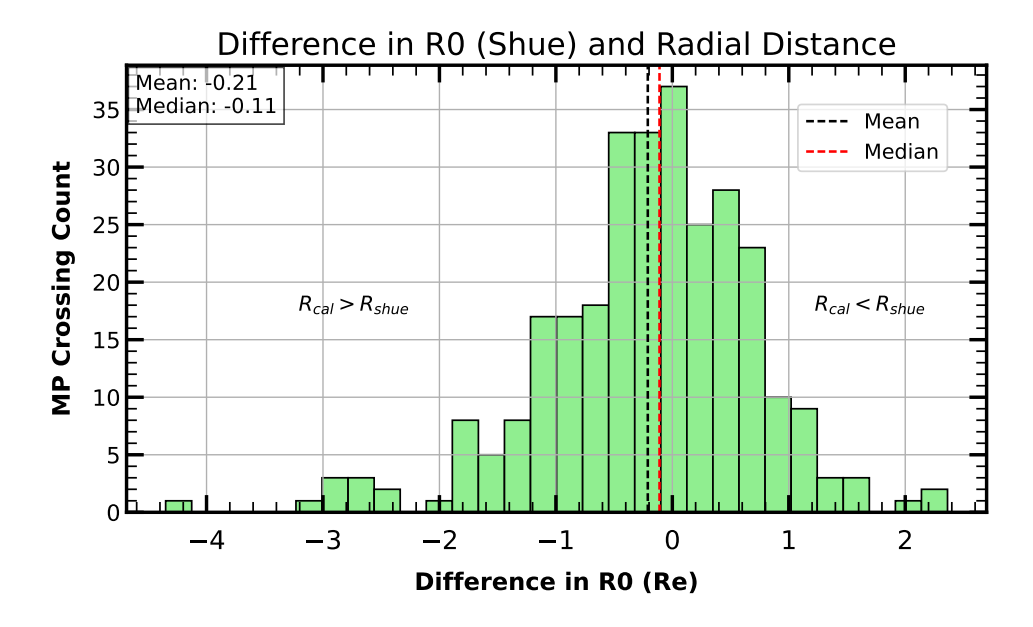


Figure 4.17: The x-axis represents "Difference in R0 (Re)" which measures the discrepancy between observed Magnetopause crossings and those predicted by the Shue model.

model and observed crossings. The distribution shows a longer tail on the negative side (where Rcal > Rshue), implying more instances where the observed Magnetopause was located significantly farther from Earth than predicted by the Shue model

Out of 297 total Magnetopause crossings, 214 (approximately 72%) fall within one standard deviation (0.92 Re) of the model-detected difference, indicating good agreement in the majority of cases. However, the crossings with larger discrepancies are often those with higher Y-axis values, where the Shue98 model performs poorly due to its reliance solely on solar wind dynamic pressure. The mean of the distribution is -0.21 Re, and the median is -0.11 Re, indicating that the model generally overestimates the standoff distance compared to actual observations, with most observed Magnetopause crossings occurring near to Earth than the Shue model predicts.

Chapter 5

Summary

In this study, we investigate the dynamic behavior of Earth's magnetopause, the boundary that separates the Earth's magnetosphere from the solar wind, particularly during solar storms, using high-resolution data from NASA's Magnetospheric Multiscale (MMS) mission. The focus is on understanding how solar phenomena, such as solar winds, affect the magnetopause's location, structure, and plasma properties. Both storm and quiescent periods are analyzed to capture the full range of magnetopause responses. Advanced analytical techniques, including minimum variance analysis, are employed to determine the magnetopause's normal direction and to project magnetic field components during boundary crossings. These findings are crucial for understanding space weather's effects on technological systems and for enhancing predictive models of magnetospheric dynamics.

Space weather, driven by solar activity, can disrupt satellites, power grids, and communication systems. Significant solar events, such as the Carrington Event (1859), the 1989 Quebec blackout, and the 2022 Starlink satellite loss, emphasize the vulnerability of modern technology to geomagnetic disturbances. The Magnetosphere of the Earth acts as a protective shield, with the magnetopause serving as its dynamic interface. The position and shape of the magnetopause are influenced by a balance between the dynamic pressure of the solar wind and Earth's magnetic pressure, making it highly sensitive to changes in solar wind intensity and the orientation of the interplanetary magnetic field (IMF).

The MMS mission, consisting of four identical spacecraft flying in a

tetrahedral formation, enables three-dimensional measurements of magnetic reconnection and boundary dynamics. Key instruments on the spacecraft include fluxgate magnetometers for measuring magnetic fields, the Fast Plasma Investigation (FPI) for capturing high-resolution plasma velocity distributions, and the Hot Plasma Composition Analyzer (HPCA) for determining ion species and energies. The orbits of the MMS satellites are optimized for frequent magnetopause crossings, providing comprehensive coverage of the boundary under various solar wind conditions.

To detect magnetopause crossings, we developed a semi automated Python pipeline that identifies abrupt changes in magnetic field and energy spectrum. Minimum variance analysis was used to determine the normal direction of the boundary, and the empirical Shue et al. (1998) model was employed to characterize the magnetopause's shape and standoff distance as functions of solar wind dynamic pressure and IMF Bz.

On quiet days, the magnetopause is located farther from Earth (e.g., 11.08 Earth radii), with smooth transitions in magnetic field and plasma parameters. During intense storm periods, such as the May 2024 "Mother's Day Storm", the magnetopause was compressed dramatically, observed as close as 6.48 Earth radii—a shift of over 3.5 Earth radii compared to the standoff distance under normal conditions. Plasma measurements showed increased turbulence, sharp density and temperature gradients, and significant magnetic field fluctuations during these crossings.

A statistical analysis over three years revealed 297 magnetopause crossings, with most observed locations falling within ±1 Earth radius of the Shue model predictions. This validates the model's utility but also highlights deviations under extreme conditions. While the subsolar magnetopause location generally aligns with model values, discrepancies are more pronounced during high solar wind pressure or strong southward IMF.

The thesis concludes that continuous, high-resolution in-situ measurements are essential for understanding the dynamic response of Earth's magnetopause to solar storms. These results are vital for space weather forecasting and the protection of technological infrastructure. The research also recommends further development of analytical and machine learning techniques to improve the detection and characterization of magnetopause

crossings, especially during extreme events. Overall, this work advances our understanding of the mechanisms governing solar wind-magnetosphere interactions and provides valuable insights for future studies and operational space weather monitoring.

5.1 Future Aspects

This study examines the displacement of the magnetopause under varying space weather conditions. Magnetopause compression has direct implications for satellite drag, satellite operations, and power grid systems, all of which are sensitive to disturbances in the near-Earth space environment. Understanding the mechanisms behind plasma depletion at the magnetopause and within the magnetosheath—such as the squeezing effect and flux tube evolution, can offer valuable insights into how solar wind energy is transferred into the magnetosphere.

Additionally, analyzing how these depletion processes vary across different phases of the solar cycle (e.g., solar maximum vs. solar minimum) can shed light on the influence of changing solar wind properties on magnetospheric dynamics. Long-term monitoring of magnetosheath fluctuations particularly in plasma density, temperature, and magnetic field strength can help clarify how solar wind variability and magnetic field orientation impact this region over time. Moreover, employing multi spacecraft observations across different parts of the magnetosheath can enhance our understanding of its three-dimensional structure and temporal evolution.

Integrating this knowledge, including magnetic reconnection, plasma instabilities, and magnetosheath behavior, into space weather forecasting models could significantly improve the prediction of geomagnetic storms and their effects on Earth's technological infrastructure. The incorporation of real-time data from missions such as MMS can further refine these models, leading to more accurate and responsive forecasting of solar wind magnetosphere interactions.

Bibliography

- D.N. Baker. What is space weather? *Advances in Space Research*, 22(1):7–16, 1998. ISSN 0273-1177. doi: https://doi.org/10.1016/S0273-1177(97)01095-8. URL https://www.sciencedirect.com/science/article/pii/S0273117797010958. Solar-Terrestrial Relations: Predicting the Effects on the Near-Earth Environment.
- DN Baker, L Riesberg, CK Pankratz, RS Panneton, BL Giles, FD Wilder, and RE Ergun. Magnetospheric multiscale instrument suite operations and data system. *Space Science Reviews*, 199:545–575, 2016.
- E Behar, F Pucci, C Simon Wedlund, P Henri, G Ballerini, L Preisser, and F Califano. Impact of solar-wind turbulence on a planetary bow shock-a global 3d simulation. *Astronomy & Astrophysics*, 692:A53, 2024.
- Laurence James Cahill and PG Amazeen. The boundary of the geomagnetic field. *Journal of Geophysical Research*, 68(7):1835–1843, 1963.
- Tong Dang, Xiaolei Li, Bingxian Luo, Ruoxi Li, Binzheng Zhang, Kevin Pham, Dexin Ren, Xuetao Chen, Jiuhou Lei, and Yuming Wang. Unveiling the space weather during the starlink satellites destruction event on 4 february 2022. *Space weather*, 20(8):e2022SW003152, 2022.
- AJ Dessler and JA Fejer. Interpretation of kp index and m-region geomagnetic storms. *Planetary and Space Science*, 11(5):505–511, 1963.
- James W Dungey. Interplanetary magnetic field and the auroral zones. *Physical Review Letters*, 6(2):47, 1961.

- MW Dunlop, TI Woodward, and CJ Farrugia. Minimum variance analysis: Cluster themes. In *Proceedings of the Cluster Workshops, Data Analysis Tools and Physical Measurements and Mission-Oriented Theory*, volume 371, page 33, 1995.
- BL Giles, JL Burch, RB Torbert, and TE Moore. Magnetospheric multiscale overview and science objectives. 2015.
- Nat Gopalswamy. Solar energetic particle events and radio bursts. *arXiv* preprint arXiv:2410.08690, 2024.
- Arthur Grönlund. Statistical survey of earth's magnetopause using mms data: Pressure balance, total pressure contributions and magnetopause velocity near the subsolar point, dawn-and dusk flanks, 2021.
- Stein Haaland, Götz Paschmann, M Øieroset, T Phan, Hiroshi Hasegawa, SA Fuselier, Vlad Constantinescu, Stefan Eriksson, Karlheinz J Trattner, Sid Fadanelli, et al. Characteristics of the flank magnetopause: Mms results. *Journal of Geophysical Research: Space Physics*, 125(3): e2019JA027623, 2020.
- Hisashi Hayakawa, Yusuke Ebihara, Alexander Mishev, Sergey Koldobskiy, Kanya Kusano, Sabrina Bechet, Seiji Yashiro, Kazumasa Iwai, Atsuki Shinbori, Kalevi Mursula, Fusa Miyake, Daikou Shiota, Marcos V. D. Silveira, Robert Stuart, Denny M. Oliveira, Sachiko Akiyama, Kouji Ohnishi, Vincent Ledvina, and Yoshizumi Miyoshi. The solar and geomagnetic storms in may 2024: A flash data report, 2024. URL https://arxiv.org/abs/2407.07665.
- Walter Heikkila. Earth's magnetosphere: Formed by the low-latitude boundary layer. Elsevier, 2011.
- Masafumi Hirahara, Tomomi Takei, Shoichiro Yokota, and Tomoki Yanagimachi. Triple-dome electrostatic energy analyzer with 360° field-of-view for simultaneous measurements of ions and electrons. *Journal of Geophysical Research: Space Physics*, 128(10):e2023JA031423, 2023.

- Sanjay Kumar and Tuija I Pulkkinen. Statistical analysis of magnetopause response during substorm phases. In *Annales Geophysicae*, volume 43, pages 137–149. Copernicus Publications Göttingen, Germany, 2025.
- J.A. Lazzús and I. Salfate. Report on the effects of the may 2024 mother's day geomagnetic storm observed from chile. *Journal of Atmospheric and Solar-Terrestrial Physics*, 261:106304, 2024. ISSN 1364-6826. doi: https://doi.org/10.1016/j.jastp.2024.106304. URL https://www.sciencedirect.com/science/article/pii/S1364682624001329.
- RP Lepping, MH Acũna, LF Burlaga, WM Farrell, JA Slavin, KH Schatten, F Mariani, NF Ness, FM Neubauer, YC Whang, et al. The wind magnetic field investigation. *Space Science Reviews*, 71:207–229, 1995.
- EA Lucek, D Constantinescu, ML Goldstein, J Pickett, Jean-Louis Pincon, F Sahraoui, RA Treumann, and SN Walker. The magnetosheath. *Space Science Reviews*, 118:95–152, 2005.
- James E Midgley and Leverett Davis Jr. Calculation by a moment technique of the perturbation of the geomagnetic field by the solar wind. *Journal of Geophysical Research*, 68(18):5111–5123, 1963.
- TKM Nakamura, KA Blasl, Y-H Liu, and SA Peery. Diffusive plasma transport by the magnetopause kelvin-helmholtz instability during southward imf. *Frontiers in Astronomy and Space Sciences*, 8:809045, 2022.
- KW Ogilvie, DJ Chornay, RJ Fritzenreiter, F Hunsaker, J Keller, J Lobell, G Miller, JD Scudder, EC Sittler, RB Torbert, et al. Swe, a comprehensive plasma instrument for the wind spacecraft. *Space Science Reviews*, 71: 55–77, 1995.
- SM Petrinec. The location of the earth's bow shock. *Planetary and Space Science*, 50(5-6):541–547, 2002.
- Viviane Pierrard, Alexandre Winant, Edith Botek, and Maximilien Péters de Bonhome. The mother's day solar storm of 11 may 2024 and its effect on earth's radiation belts. *Universe*, 10(10):391, 2024.

- Edmond C Roelof and David G Sibeck. Magnetopause shape as a bivariate function of interplanetary magnetic field bz and solar wind dynamic pressure. *Journal of Geophysical Research: Space Physics*, 98(A12): 21421–21450, 1993.
- C. T. Russell, B. J. Anderson, W. Baumjohann, K. R. Bromund, D. Dearborn, D. Fischer, G. Le, H. K. Leinweber, D. Leneman, W. Magnes, J. D. Means, M. B. Moldwin, R. Nakamura, D. Pierce, F. Plaschke, K. M. Rowe, J. A. Slavin, R. J. Strangeway, R. Torbert, C. Hagen, I. Jernej, A. Valavanoglou, and I. Richter. The magnetospheric multiscale magnetometers. *Space Science Reviews*, 199(1–4):189–256, August 2014. ISSN 1572-9672. doi: 10.1007/s11214-014-0057-3. URL http://dx.doi.org/10.1007/s11214-014-0057-3.
- J-H Shue, JK Chao, HC Fu, CT Russell, P Song, KK Khurana, and HJ Singer. A new functional form to study the solar wind control of the magnetopause size and shape. *Journal of Geophysical Research: Space Physics*, 102(A5):9497–9511, 1997.
- R Smets, G Belmont, D Delcourt, and L Rezeau. Diffusion at the earth magnetopause: enhancement by kelvin-helmholtz instability. In *Annales Geophysicae*, volume 25, pages 271–282. Copernicus Publications Göttingen, Germany, 2007.
- CP Sonett and IJ Abrams. The distant geomagnetic field: 3. disorder and shocks in the magnetopause. *Journal of Geophysical Research*, 68(5): 1233–1263, 1963.
- P Song, CT Russell, JT Gosling, M Thomsen, and RC Elphic. Observations of the density profile in the magnetosheath near the stagnation streamline. *Geophysical research letters*, 17(11):2035–2038, 1990.
- KA Sorathia, VG Merkin, EV Panov, B Zhang, JG Lyon, J Garretson, AY Ukhorskiy, S Ohtani, M Sitnov, and M Wiltberger. Ballooning-interchange instability in the near-earth plasma sheet and auroral beads: Global magnetospheric modeling at the limit of the mhd approximation. *Geophysical Research Letters*, 47(14):e2020GL088227, 2020.

- John R Spreiter and SS Stahara. The location of planetary bow shocks: A critical overview of theory and observations. *Advances in Space Research*, 15(8-9):433–449, 1995.
- Lucile Turc, Owen Wyn Roberts, Daniel Verscharen, Andrew P Dimmock, P Kajdič, Minna Palmroth, Yann Pfau-Kempf, Andreas Johlander, Maxime Dubart, Emilia KJ Kilpua, et al. Transmission of foreshock waves through earth's bow shock. *Nature Physics*, 19(1):78–86, 2023.
- D. M. Willis. The microstructure of the magnetopause. *Geophysical Journal International*, 41(3):355–389, 06 1975. ISSN 0956-540X. doi: 10.1111/j.1365-246X.1975.tb01621.x. URL https://doi.org/10.1111/j.1365-246X.1975.tb01621.x.
- BJ Zwan and RA Wolf. Depletion of solar wind plasma near a planetary boundary. *Journal of Geophysical Research*, 81(10):1636–1648, 1976.